Michael Selig,[1,2,3,4] *Boris Lorenz,*[1,5] *Dirk Henrichmöller,*[6] *Karsten Schmidt,*[2] *Andrew Ball,*[3] *and Bo Persson*[1,5]

Rubber Friction and Tire Dynamics: A Comparison of Theory with Experimental Data

REFERENCE: Selig, M., Lorenz, B., Henrichmöller, D., Schmidt, K., Ball, A., and Persson, B. N. J., **"Rubber Friction and Tire Dynamics: A Comparison of Theory with Experimental Data,"** *Tire Science and Technology*, TSTCA, Vol. 42, No. 4, October–December 2014, pp. 216–262.

ABSTRACT: In this contribution, a simple rubber friction law is presented. The model can be used for tire and vehicle dynamics calculations [*19*]. The friction law is tested by comparing numerical results to the full rubber friction theory [*6*] and to experimental data.

A two-dimensional tire model is introduced. The model combines the rubber friction law with a simple mass-spring description of the tire body. The tire model is very flexible and can be applied to different maneuvers. It can be used for calculating μ-slip curves, the self-aligning torque, braking and cornering, or combined motion (e.g., braking during cornering). The theory predictions are compared to measured data from indoor tire testing on sandpaper substrate. Simulations of antilock braking systems (ABS) using two different control algorithms are also presented.

KEY WORDS: rubber friction, tire dynamics, tire model, tire measurement, ABS

Introduction

Rubber friction is a crucial topic, especially for practical applications. Examples are tires, wiper blades, rubber seals, syringes, or conveyor belts [*1–18*]. In most theoretical studies, rubber friction is described using very simple phenomenological models, e.g., the Coulomb friction law with a friction coefficient, which may depend on the local sliding velocity. However, rubber friction depends on the *history* of the sliding motion (memory effects). As we have shown previously [*6*], memory effects are very important for an accurate description of rubber friction. When rubber is sliding on a hard rough substrate, the history dependency of friction is mainly due to frictional heating in the rubber-substrate contact regions. Many experimental studies have shown the influence of frictional heating on rubber friction as an apparent dependence of the rubber friction on the normal load.

Many articles have been published related to tire dynamics, e.g., in the context of antilock braking models. The central point in tire dynamics is the

[1] *PGI-1, FZ-Jülich, D-52425 Jülich, Germany*
[2] *Frankfurt University of Applied Sciences, Frankfurt am Main, Germany*
[3] *University of Huddersfield, Huddersfield, United Kingdom*
[4] Corresponding author
[5] www.multiscaleconsulting.com
[6] *ika, RWTH Aachen University, Aachen, Germany*

road-tire interaction, thus the rubber friction. Hence, unless this friction is accurately described, no tire model will provide an accurate picture of the tire dynamics, independent of the tire-body description detail level. Usually, the road-tire friction is described only in a very approximate way. Many sophisticated finite element models for tire dynamics describe the frictional interaction only via a static and a kinetic rubber friction coefficient. In other studies, the dynamic behavior of the whole tire is described by simply using interpolation formulas. The most famous example is the well-established "Magic Formula" [*4*]. However, this approach requires a very large set of measurements to characterize the tire properties and is very expensive and time-consuming. In addition, it can not describe the influence of the sliding history (memory effects) on tire dynamics.

In section Rubber Friction, we present a general introduction to rubber friction. Under Phenomenological Rubber Friction Law, we propose a very simple rubber friction law that includes memory effects. The simplified model gives almost identical results as the full model [see *6*,*19*]. Under Rubber Compound Viscoelastic Modulus and Surface Roughness Power Spectrum, we present experimental results for the tread rubber viscoelastic modulus and the surface roughness power spectrum of the sandpaper road track, respectively, used in our study. Under 1D Tire Model, we compare the results of a simple one-dimensional (1D) tire model with experimental data. Under 2D Tire Model, a two-dimensional (2D) tire model is presented where the rubber-road friction theory (including the flash temperature effect) is combined with a simple 2D description of the tire body. We assume that the most important aspect of the tire body is its distributed mass and elasticity, both of which are fully considered in the model. An advantage of the 2D model over a full three-dimensional (3D) model is that any footprint pressure distribution, e.g., a measured pressure distribution, can be easily imposed. In a 3D tire model, the pressure distribution is fixed by the model itself. As shown in Ref. [*6*], the 2D tire model allows explicit studies on the sensitivity of the tire dynamics to the characteristics of the footprint pressure distribution. In section ABS Braking Simulations, we also present simulations of antilock braking system (ABS) braking using two different control algorithms. We end with Summary and Conclusions.

Rubber Friction

Rubber friction depends on the history of the sliding motion, because the temperature in the rubber-road asperity contact regions at time t depends on the sliding history for all earlier times $t' < t$ due to frictional heating. This dependency is called memory effect, which is essential for an accurate description of rubber friction. The effect is illustrated in Figs. 1 and 2 for rubber tread blocks sliding on different surfaces. The calculated kinetic friction

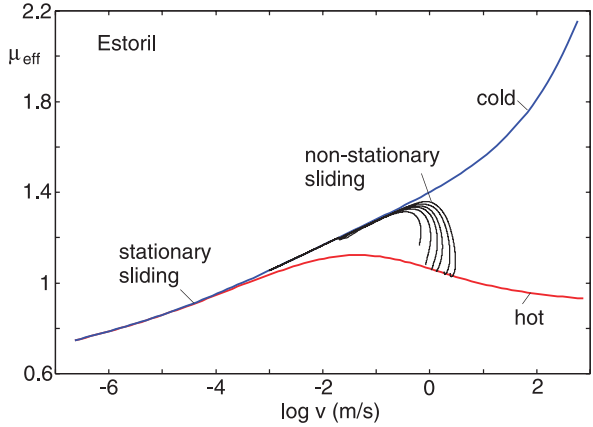

FIG. 1 — *Kinetic friction coefficient (stationary sliding) as a function of the logarithm (with 10 as basis) of the sliding velocity for a tread rubber on an asphalt road surface. The blue line, marked cold, is without the flash temperature. The red line, marked hot, is including the flash temperature. The black curves are showing the effective friction, experienced by a tread block, when it goes through the footprint, for the car velocity of 27 m/s and for several slip values (0.005, 0.0075, 0.01, 0.03, 0.05, 0.07, and 0.09). The experienced friction of the tread block follows first the cold rubber branch of the steady-state kinetic friction coefficient. And after, when the block has slipped a distance of order the diameter of the macroasperity contact region, and the flash temperature has fully evolved, the hot rubber branch is followed.*

coefficient for stationary sliding without flash temperature is shown by the blue curve, whereas the red curve includes the flash temperature, as a function of the velocity v of the bottom surface of the rubber block. The black lines represent the effective friction during nonstationary sliding, experienced by a rubber tread

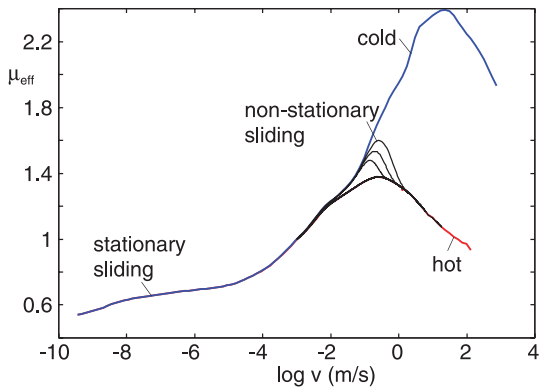

FIG. 2 — *Kinetic friction coefficient (nonstationary sliding) as a function of the logarithm (with 10 as basis) of the sliding velocity for a sandpaper surface and a different rubber compound than in Fig. 1 for a car velocity of 16.66 m/s and for several slip values (0.07, 0.15, and 0.8). The experienced friction of the tread block follows first the cold rubber branch of the steady-state kinetic friction coefficient. Then, when the block has slipped a distance of order the diameter of the macroasperity contact region, the hot rubber branch is followed.*

block during braking at various slips. Note that some finite sliding distance is necessary to fully develop the flash temperature effect. The initial friction acting on the tread block follows the blue curve according to "cold-rubber." In this case, the flash temperature is negligible. For larger slip distances the friction follows the hot branch (red curve). Therefore, it is not possible to describe rubber friction accurately using only a static and a kinetic friction coefficient, as is usually done even in advanced finite-element tire dynamics models. In fact, as shown above, the friction cannot even be described by a function $\mu(v)$ that depends on the instantaneous sliding velocity $v(t)$, but the friction depends on $v(t')$ for all times $t' \leq t$ (memory effect).

The results in Fig. 1 are for a tire on an asphalt road surface, where the so-called macroasperity contact regions (see below) are relatively large, because of the large sand particles on the road surface. For other substrates, such as safety walk or sandpaper, the size of the macroasperity contact regions can be very small. In this case, even a very small slip distance will result in motion along the hot-rubber branch. This is illustrated in Fig. 2 for nonstationary sliding experienced by a rubber tread block during braking at various slip values (0.07, 0.15, and 0.8) on the sandpaper corundum P80 substrate used in the tire dynamics measurements presented later.

To give a preparation to what follows, the rubber friction theory is reviewed. More details are given in Refs. [*5*,*6*]. In the theory, the road asperities cause viscoelastic deformations of the rubber surface that result in energy dissipation. An asperity contact region with the diameter d generates time-dependent (pulsating) deformations of the rubber. The deformation is characterized by the frequency $\omega = v/d$, where v is the sliding velocity. The viscoelastic deformations, and most of the energy dissipation, extend into the rubber by a characteristic distance of order d. Therefore, most of the energy dissipation occurs in a volume element of order d^3. To have a large asperity-induced contribution to the friction, the frequency ω should be close to the maximum of the $\tan\delta = \text{Im}\, E(\omega)/\text{Re}\, E(\omega)$ curve. Here, $E(\omega)$ is the viscoelastic modulus of the rubber. In reality, there will be a wide distribution of asperity contact sizes. This means that there will be a wide range of deformation frequencies, lets say, from ω_0 to ω_1, as shown in Fig. 3. A large friction requires, that $\tan\delta$ is as big as possible for all these frequencies.

Usually, the viscoelastic modulus of rubber-like materials depends strongly on the temperature T. An increase in temperature by 10°C may shift the $\tan\delta$ curve to higher frequencies with one frequency decade. In general, this will reduce the viscoelastic contribution to the rubber friction, as shown in Fig. 3.

The distribution of asperity sizes is usually very wide for real surfaces. A good picture of a rough surface is to think about it as big asperities on top of which occur smaller asperities on top of which occur even smaller asperities, and so on. This is shown in Fig. 4, where roughness occurs on two length scales. To obtain the total energy dissipation during sliding on a real surface, the sum of

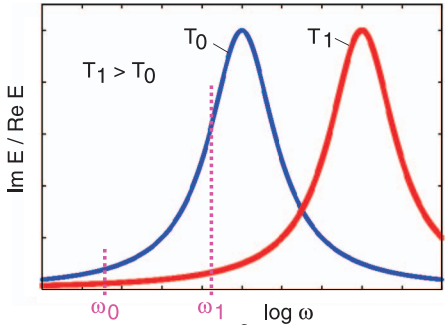

FIG. 3 — *When the temperature increases, the tan* $\delta = Im\mathrm{E}/Re\mathrm{E}$ *spectrum shifts to higher frequencies. In general, this results in a decrease of the viscoelastic contribution to the rubber friction. It is assumed that the road asperities cause pulsating frequencies in the range between* ω_0 *and* ω_1.

the contribution from asperity-induced deformations of the rubber on all relevant length scales is needed. Note that different decades in length scales may be equally important [*5*].

Temperature has a significant influence on rubber friction. The most important contribution to rubber friction is the viscoelastic energy dissipation. Viscoelastic energy dissipation results in local heating of the rubber in the region where the energy dissipation occurs leading to local temperature increases that become larger when smaller and smaller asperity contact regions are observed. This in time and space local temperature increase is referred to as the *flash temperature*. The flash temperature has an extremely significant effect on the rubber friction, as illustrated in Figs. 1 and 2, wherein the calculated steady-state kinetic friction coefficient is shown, when a block of tread rubber is sliding on an asphalt road surface. The upper curve is the result without taking the flash temperature into account. This means the temperature is assumed to be the same as the background temperature T_0 everywhere. The lower curve includes the flash temperature. Note that for sliding velocities $v > 0.001$ m/s, the flash temperature results in a decrease of the sliding friction. For velocities v

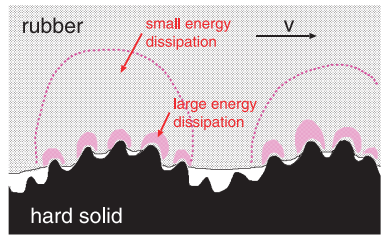

FIG. 4 — *Energy dissipation per unit volume. It is highest in the smallest asperity contact regions.*

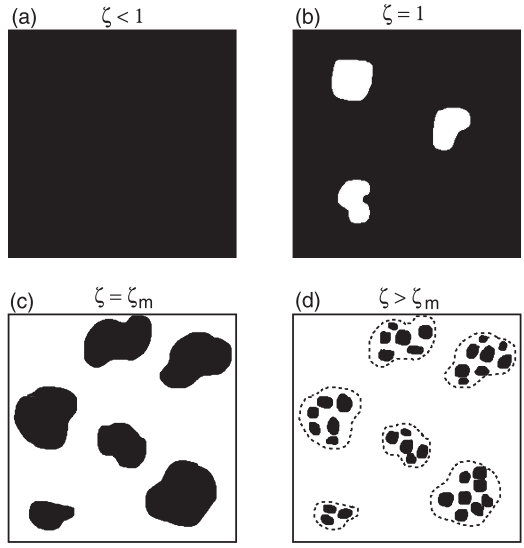

FIG. 5 — *Contact region between a tire and a road surface. At low magnification $\zeta < 1$, it appears that the tire is in complete contact with the road. But increasing the magnification, the contact area decreases continuously, as indicated in the figure.*

< 0.001 m/s, the produced heat has enough time to diffuse away from the asperity contact regions, resulting in a negligible flash temperature effect.

The concept of the macroasperity contact region is very important for the rubber friction theory. Studying the footprint contact region between a tire and a road surface at different magnifications ζ shows the following: at low magnification, the road surface seems smooth and the contact between the tire and the road appears to be complete within the footprint area. This is illustrated in Fig. 5a. However, increasing ζ, noncontact regions can be detected (Fig. 5b). At high enough magnification, isolated contact regions can be observed (Fig. 5c). When the magnification increases even further, contact regions break up into even smaller contact regions (Fig. 5d). We denote the contact regions observed in Fig. 5c as the macroasperity contact regions with the average diameter D while the corresponding magnification is denoted by ζ_c. Formally, ζ_c is defined to be the magnification where the second derivative of $\log P(\zeta)$ with respect to $\log \zeta$ has its first maximum with increasing ζ (see [*6*,*20*]). When the nominal pressure in the tire-road contact region is small enough, the macroasperity contact regions are well separated. But the separation between the microasperity contact regions within the macroasperity contact regions are in general rather small. When the flash temperature effect is calculated, the produced heat by the microasperity contact regions is smeared out uniformly within the macroasperity contact regions. For road surfaces $D \approx$

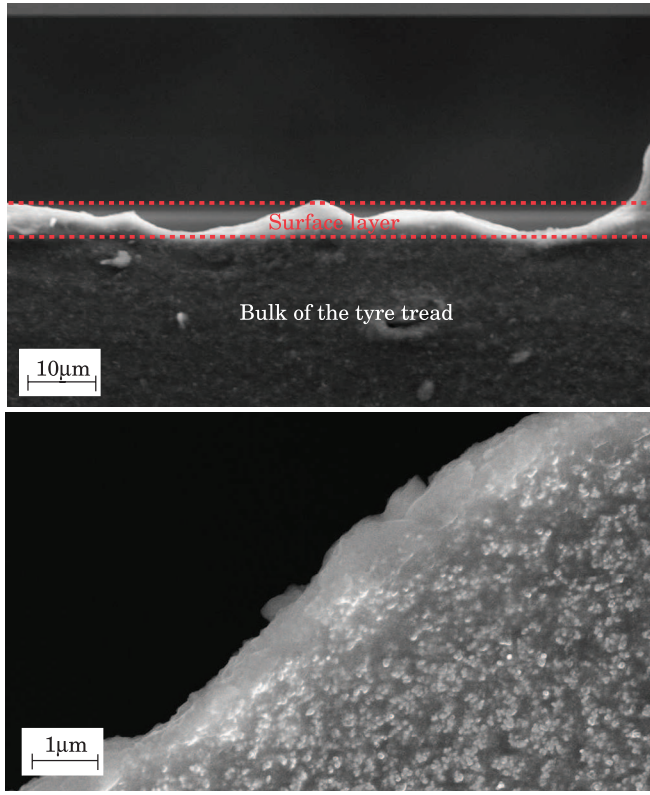

FIG. 6 — *Scanning electron microscopy images of the surface region of a car tire tread block at low magnification (top) and at higher magnification (bottom). Acknowledgment is made to Marc Masen, Imperial College London, for providing the images.*

0.1–1 cm, and the fraction of the tread block surface occupied by the macroasperity contact regions is typically between 10 and 30%.

It is assumed that only the surface roughness with wavevectors $q < q_1$ has a contribution to the friction in the theory developed in Ref. [*6*]. For clean road surfaces, the cut-off wavevector q_1 is determined by degradation of material. That is, the local stress and temperature in the asperity contact regions on the length scale $1/q_1$ are so high that the rubber bonds break, resulting in a thin modified (dead) layer of rubber at the surface region of thickness $\approx 1/q_1$. In another approach by Kluppel and Heinrich [*8*], a different mechanism for obtaining q_1 is presented.

Modified surface layers have indeed been detected on rubber tread blocks [*21*]. In Fig. 6, we show scanning electron microscopy images of the surface region of a tire tread block at two different magnifications. In the high-magnification image (bottom), a ≈ 1 μm thick layer of modified rubber can be

observed. Note that in this layer, no filler particles (carbon black) can be observed. Energy-dispersive x-ray spectroscopy analysis showed an increased concentration of oxygen compared to the bulk material. The increase of oxygen in the surface region suggests that the rubber reacts chemically with the environment and is undergoing oxidation processes during sliding. This is indeed expected because of the high (flash) temperatures and large stresses in the rubber-road asperity contact regions during slip. Using indentation experiments [*21*], the viscoelastic properties of the modified surface layer were studied, showing that the surface layer is much softer than the bulk, with a long-time (relaxed) modulus $\approx$1000 times smaller than in the bulk, whereas the short-time response indicated an $\approx$5 times softer surface layer. Furthermore, the viscoelastic spectral density exhibited much slower relaxation processes (longer relaxation times) than in the bulk. From this, the following can be concluded:

(1) The rubber friction after run-in is rather insensitive to the road surface roughness on clean roads. This has been found in different experimental studies (see [*22*]) and can be understood as follows. The cut-off q_1 on surfaces with smoother and less sharp roughness, or for surfaces where the roughness occurs at shorter length scales, will be larger, i.e., the cut-off wavelength $\lambda_1 = 2\pi/q_1$ will be smaller than for road surfaces with larger roughness in such a way that the temperature and stress increase in the asperity contact regions observed at the resolution λ_1 or magnification $\zeta = q_1/q_0$ are roughly the same on all surfaces. This means that a larger range of roughness will contribute to the rubber friction on "smoother" surfaces compared to rougher surfaces. From this, it follows that the friction after run-in may vary much less between different clean road surfaces than expected from the variation of the magnitude of the surface roughness.
(2) The cut-off q_1 may be determined by the nature of the road surface contamination. In this case, if the cut-off is fixed, e.g., by the size of the contamination particles, a much larger change in the friction coefficient can be observed between different road surfaces, and for tires with different types of tread rubber.

For clean surfaces, q_1 is determined by the thickness of a thin modified (dead) layer (see Fig. 6) that is generated by the high stresses and temperatures at the tread rubber surface during run-in. This process is likely also related to rubber wear. Rubber wear occurs during slip and leads to a contamination of the track by small wear elements. This may have some effect on the sliding friction. It is also well known to occur when a car brakes or accelerates on a road, leaving black strips of rubber particles on the road surface. However, we do not expect that the wear particles have a large effect on the investigated friction. This is because most of them are of similar size as the cut-off distance. During

moderate slip, the particles only cover a small part of the road surface. Also, this statement is supported by our laboratory experiments where we observed a negligible change in the rubber friction force, when the same rubber tread element, or rubber block slides a second time on the same, not cleaned road track, or even on a much smoother grinded steel surface.

The cut-off length $1/q_1$ depends on the rubber compound used, and also on the characteristics of the road surface. Changing the road surface requires some short run-in to form a new thin modified surface layer on the tread block, which is corresponding to a new cut-off length.

We have derived a set of equations describing the viscoelastic contribution to the friction acting on a rubber block squeezed with the stress σ_0 against a hard randomly rough surface [*6*]. Here, we summarize the basic equations. There are two contributions to the frictional stress $\sigma_f = \mu(t)\ \sigma_0$. One contribution is the dissipation of energy inside the rubber, due to viscoelasticity of the rubber material. This depends on the history of the sliding motion [velocity $v(t) = \dot{x}(t)$] expressed via the following series of equations:

$$\mu(t) \approx \frac{1}{2}\int_{q_0}^{q_1} dq\, q^3\, C(q) P(q,t) \int_0^{2\pi} d\phi \cos\phi\, \mathrm{Im}\frac{E(qv(t)\cos\phi, T_q(t))}{(1-\nu^2)\sigma_0}.$$

The flash temperature at time t enters in as

$$T_q(t) = T_0 + \int_0^t dt'\, \Gamma(t,t') \int_{q_0}^{q_1} dq' f(q',t')$$

$$\times \frac{1}{\pi}\int_0^\infty dk\, \frac{4q^2}{k^2+4q^2}\, \frac{4q'}{k^2+4q'^2} e^{-Dk^2(t-t')},$$

where $\Gamma(t, t') = h(w(t, t'))$ with

$$h(w) = 1 - \frac{2}{\pi} w(1-w^2)^{1/2} - \frac{2}{\pi}\arcsin w,$$

for $w < 1$ and $h(w) = 0$ for $w > 1$. Here, $w(t, t') = [x(t) - x(t')]/2R$ depends on the history of the sliding motion. The function

$$f(q,t) = \frac{v(t)}{\rho C_v} q^4 C(q) \frac{P(q,t)}{P(q_m,t)} \int_0^{2\pi} d\phi \cos\phi\, \mathrm{Im}\frac{E(qv(t)\cos\phi, T_q(t))}{1-\nu^2},$$

where $v = \dot{x}(t)$ depends on time. The function $P(q, t)$ (which also depends on time) is represented by

$$P(q,t) = \frac{2}{\pi}\int_0^\infty dx\, \frac{\sin x}{x} \exp\left[-x^2 G(q,t)\right] = \mathrm{erf}\left(\frac{1}{2\sqrt{G}}\right),$$

where

$$G(q,t) = \frac{1}{8}\int_{q_0}^{q} dq\, q^3 C(q) \int_0^{2\pi} d\phi \left| \frac{E(qv(t)\cos\phi, T_q(t))}{(1-\nu^2)\sigma_0} \right|^2 .$$

The second contribution to the rubber friction is deduced from the area of (apparent) contact observed at the magnification ζ_1 and is given by $\tau_f A_1/A_0$. Here, $\tau_f(v)$ is the effective frictional shear stress acting in the contact area $A_1 = A(\zeta_1) = P(q_1, t)$. This theory is denoted as the "full theory."

Phenomenological Rubber Friction Law

In automotive tire applications, for a slip between 5 and 10% and a typical footprint length of 10 cm, the slip distance of a tread rubber block in the footprint will be of order 1 cm. This is of order or larger than the diameter D of the macroasperity contact regions. As long as the slip distance $r(t)$ is small compared to D, the friction follows the cold rubber branch of the steady-state relation $\mu(v)$ (see blue curve in Fig. 1). So, $\mu(t) \approx \mu_{cold}(v(t))$ for the slip distance $r(t) << D$. When the tread block travels towards the end of the footprint, the slip distance $r(t)$ may be of the order of D, or larger, and the friction will follow the hot branch of the $\mu(v)$ relation. This means $\mu(t) \approx \mu_{hot}(v(t))$ for $r(t) > D$. We have found that the following history-dependent friction law [*19*] predicts almost the same friction force as the full theory presented above and in Ref. [*6*]:

$$\mu(t) = \mu_{cold}(v(t), T_0)e^{-r(t)/r_0} + \mu_{hot}(v(t), T_0)\left[1 - e^{-r(t)/r_0}\right]. \qquad (1)$$

Here, $v(t)$ is the instantaneous sliding velocity, $r(t)$ is the sliding distance, and $r_0 \approx 0.2\, D$. We denote eq 1 as the "cold-hot friction law." The length D, which is typically $\approx$ 1 mm, depends on the road surface and on the rubber compound. Applying the full friction theory, the functions μ_{cold} (v, T_0), μ_{hot} (v, T_0) and the length D can be calculated.

Let us briefly discuss the philosophy of using the friction law presented above. There are (at least) two temperature effects that differ with respect to their dependency on time t and spatial coordinate $\mathbf{x}$. The flash temperature is the sudden increase in the rubber temperature in road-rubber asperity contact regions due to the frictional heating. This effect is located in very small volume elements $\sim D^3$ and prevails for very short time periods of order $\tau = D/v$, where D is the diameter of an macroasperity contact region and v the slip velocity. In a typical case, $D \approx 1$ mm and $v \approx 1$ m/s, giving the flash temperature timescales $\tau \approx 10^{-3}$ s (or less). In addition to the flash temperature, there is a change in the rubber temperature over much longer timescales due to the rolling resistance and from the frictional energy dissipation during slip, e.g., during braking or cornering. The latter effect can be considered as the cumulative effect of the flash temperature. Both processes occur on timescales of seconds or more. So, compared to the flash temperature effect, it varies slowly in time (and space).

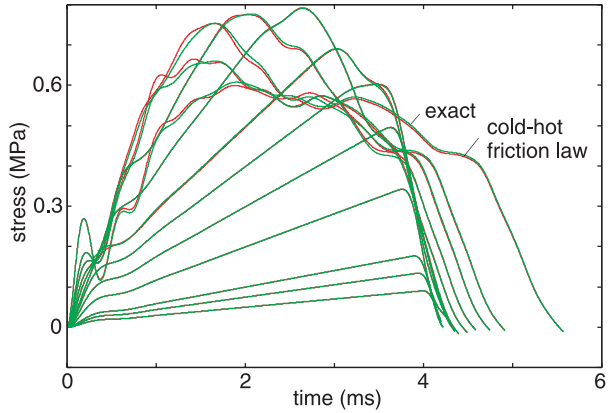

FIG. 7 — *Frictional shear stress acting on a tread block as a function of time for many slip values (0.005, 0.0075, 0.01, 0.03, 0.05, 0.07, 0.09, 0.12, 0.15, and 0.25). Car velocity 27 m/s and tire background temperature* $T_0 = 60°C$. *1D tire model using the full friction model (green curves) and the cold-hot friction law (eq 1) (red curves). Passenger car tread compound.*

We refer to this slowly varying temperature as the background temperature and denote it as $T_0(t)$. Note that $T_0(t)$ depends on the driving history over long periods (from seconds to hours) and can only be determined by performing full vehicle dynamics experiments or simulations taking into account the external conditions such as wet or dry road, road and air temperature, and humidity. We also note that there are temperature effects that occur on other timescales associated with the interaction between hot spots (see *Discussion* under 2D Tire Model) (involving short times), or that are associated with the time period of the tire rolling one orbit [with the characteristic time $2\,\pi\,R/v \approx 0.1$ s (R is the tire radius) in a typical case]. The latter effect could also be considered as part of the background temperature.

The temperature T_0 in $\mu_{hot}\,(v, T_0)$ is the background temperature discussed above. The flash temperature is already accounted for and determines (or influences) the velocity dependency of $\mu_{hot}\,(v, T_0)$. The function $\mu_{cold}\,(v, T_0)$ is the friction coefficient at the background temperature T_0 neglecting the flash temperature effect.

To illustrate the accuracy of the cold-hot rubber friction law (eq 1), the dynamics of one tread block is analyzed as it travels through the tire-road footprint. The frictional shear stress acting on this tread block as a function of time for many slip values (0.005, 0.0075, 0.01, 0.03, 0.05, 0.07, 0.09, 0.12, 0.15, and 0.25) is shown in Fig. 7. Note that the cold-hot friction law (eq 1) (red curves) gives approximately the same result as the full friction theory (green curves). The μ-slip curve is shown in Fig. 8. The results in Figs. 7 and 8 do not include the contribution to the friction from the area of contact.

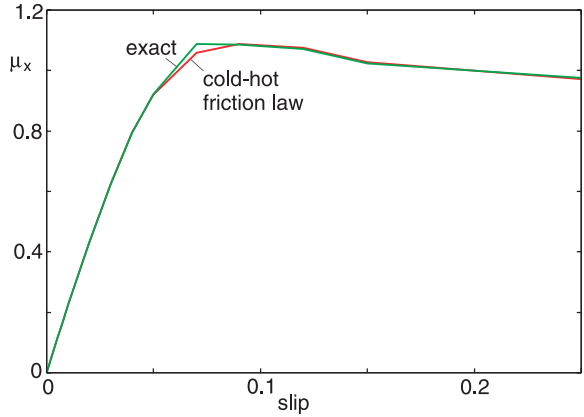

FIG. 8 — μ-*Slip curve for the 1D tire model using the full friction model (green curve) and the cold-hot friction law (eq 1) (red curve). Passenger car tread compound.*

Rubber Compound Viscoelastic Modulus

We have measured the viscoelastic modulus of the tread rubber used in the present study. In Fig. 9, we show the logarithm of the real (red) and imaginary (blue) part of the viscoelastic modulus as a function of the logarithm of the frequency of the tread rubber compound at the reference temperature $T_0 = 20°C$. The square symbols are large strain or stress results obtained from strain-sweep

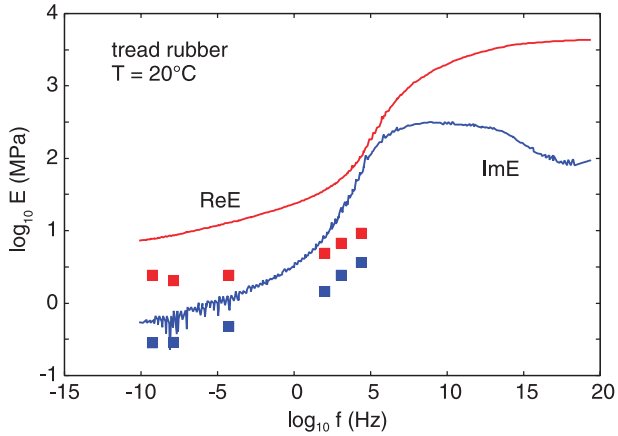

FIG. 9 — *Logarithm of the real (red) and imaginary (blue) part of the viscoelastic modulus as a function of the logarithm of the frequency of the tread rubber compound at the reference temperature* $T_0 = 20°C$. *The square symbols are large strain or stress results obtained from strain-sweep data using the self-consistent stress procedure (eq 13 in [23]) for a substrate surface with the rms slope* $\kappa = 0.7$.

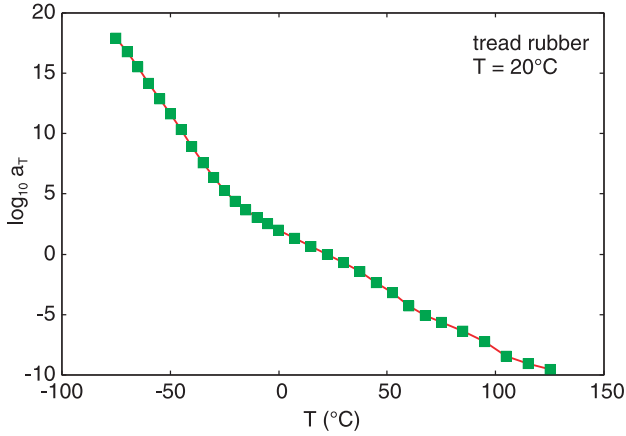

FIG. 10 — *Shift factor* a_T *as a function of the temperature* T. *The reference temperature* T = 20°C. *It is also used to shift the individual strain sweep measurements in Fig. 11.*

data using the self-consistent stress procedure (see eq 13 in [*23*]) for a substrate surface with the root mean square (rms) slope $\kappa = 0.7$. Figure 10 shows the shift factor a_T as a function of the temperature T for the same rubber compound.

In Fig. 11, we show the real part of E as a function of the applied strain during oscillation at fixed frequency of 1 Hz. The curves are obtained at different temperatures starting from 120 to –40°C.

Figure 12 shows tangent delta (tan δ) as a function of frequency for the same tread rubber compound. The red curve is for small strain (0.2%), whereas the green squares are the large strain or stress results.

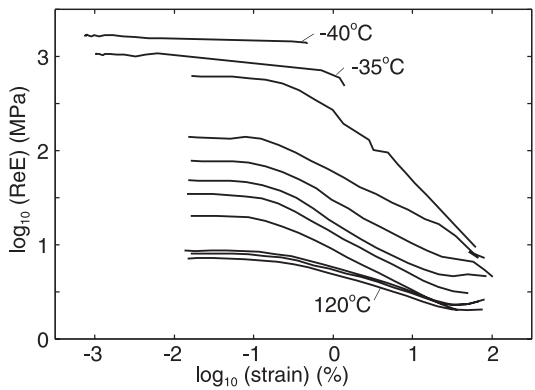

FIG. 11 — *Real part of* E *as a function of the applied strain during oscillation at fixed frequency of 1 Hz. The curves are obtained at different temperatures starting from 120 to –40°C.*

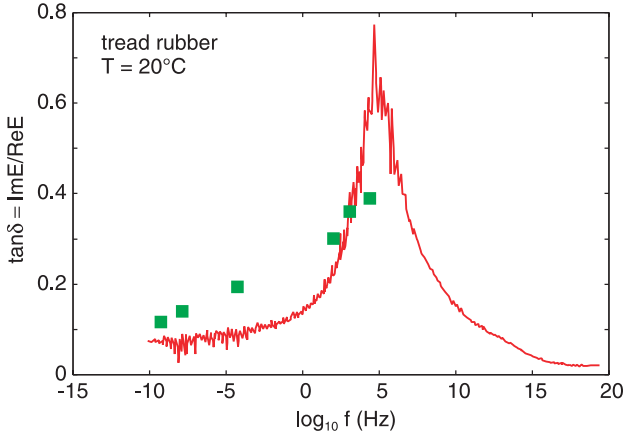

FIG. 12 — *Tan δ as a function of frequency, as obtained using experimental data for a tread rubber compound. The temperature* T = *20°C and the red curve is for small strain (0.2%). The green squares are large strain or stress results obtained from strain-sweep data using the self-consistent stress procedure (eq 13 in [23]) for a substrate surface with the rms slope* κ = *0.7.*

Surface Roughness Power Spectrum

We have measured the surface topography of the sandpaper surface used in the tire dynamics experiments. However, the measurements were done on used sandpaper when it was removed from the experimental setup after a long time of use. The surface of the sandpaper was much smoother than of new sandpaper of the same type due to wear when the tires slip over the sandpaper. The actual tire friction measurements were done some time in the middle of the lifetime of the sandpaper, and we have no direct information about the surface topography of the sandpaper at that time. We have increased the amplitude of the measured surface roughness by a factor of ≈1.18 to take into account that the roughness amplitude likely was larger at the time of the tire dynamics measurements.

Figure 13 shows the surface roughness top power spectrum on a ($\log_{10}$–$\log_{10}$ scale) of the corundum P80 sandpaper, calculated from the measured surface height profile. The long wavelength roughness was probed using a stylus instrument and gives the blue, green, and red lines in the figure, whereas the short wavelength roughness was studied using atomic force microscopy on top of some big corundum particles. The actual power spectrum used in the calculations was the measured calculation multiplied by a factor of $(1.18)^2 \approx 1.4$ to take into account the larger surface roughness expected at the time of the tire measurements.

1D Tire Model

The results presented in this section have been obtained using a 1D model of a tire shown in Fig. 14. A tread block is attached to a tire-body block that is

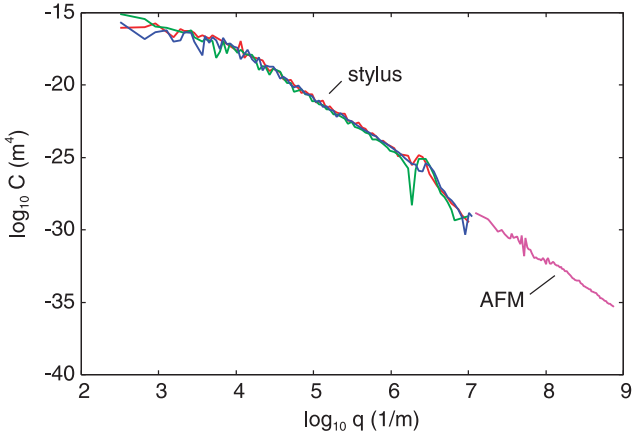

FIG. 13 — *Power spectrum for a used corundum P80 sandpaper, as a function of the wavevector* q. *The figure shows the top power spectrum on a* log_{10}–log_{10} *scale.*

connected to the rim by viscoelastic springs. The springs have both elongation and bending elasticity k (and damping γ) that are used in longitudinal (e.g., braking) or transverse (cornering) direction. We optimize the tire-body spring constant to reproduce the tire transverse (cornering) and longitudinal stiffness. The damping has been chosen so as to give a critical damping that we have found gives the best agreement with the full 2D tire model discussed under 2D Tire Model. That is $\gamma = 2(mk)^{1/2}$, where k is the (bending or elongation) spring constant, and m the mass of the tread block plus the tire-body block. The free oscillations are determined by

$$m\ddot{u} = -ku - \gamma\dot{u},$$

so we have a damped oscillator with the complex frequency

$$\omega = i\frac{\gamma}{2m} \pm \left[\frac{k}{m} - \left(\frac{\gamma}{2m}\right)^2\right]^{1/2}.$$

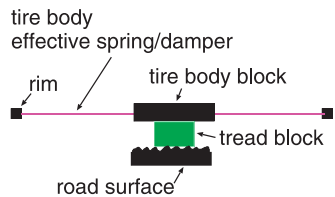

FIG. 14 — *1D model of a tire. A tread block is attached to a tire body block that is connected to the rim by viscoelastic springs. The springs have both elongation and bending elasticity (and damping) that are used in longitudinal (e.g., braking) or transverse (cornering) motion.*

The critical damped case is when the square-root term vanishes or $\gamma = 2(mk)^{1/2}$. The optimization of the tire-body (bending or elongation) spring constant k is done in an iterative way. We first calculate the (longitudinal or transverse) stiffness C_c for a given spring constant k and then replace

$$k \rightarrow k \times (C/C_c),$$

where C is the measured (longitudinal or transverse) stiffness. After a few numbers of iterations, a spring constant can be obtained that results in a calculated stiffness C_c that agrees well with the measured value C.

Numerical Results and Comparison with Experimental Data

In this section, we compare the μ-slip and μ-slipangle curves, calculated using the 1D tire model, to experimental data. Under 2D Tire Model, we show that the 2D tire model gives very similar results. However, the 2D tire model calculations are much more time-consuming, and we therefore focus on the 1D tire model here for comparison to experimental data.

The experimental results presented below were obtained for a passenger car summer tire with silica-based tread compound with the viscoelastic modulus given under Rubber Compound Viscoelastic Modulus. The substrate was corrundum P80 sandpaper (see Surface Roughness Power Spectrum). For all experiments, the rim-mounted tire is bolted to the measuring hub of the tire test bench. The nominal inflation pressure of the tire is adjusted, and the tire is run-in at a medium wheel load with a velocity of 60 km/h for 30 min. For preconditioning purposes, the slipangle is changed ±5°, with an angle rate of 2°/s. After a cooldown phase, the nominal inflation pressure of the tire is adjusted. During the experiments, wheel load F_N, longitudinal force F_x, lateral force F_y, aligning torque M_z, overturning torque M_x, slip and camber angle, longitudinal slip, and rolling velocity are recorded, with a sample rate of 250 Hz. For brake slip measurements, a brake torque is induced with a linear ramp function. A brake disk is used to apply the brake torque. The torque is set to zero when the rotational velocity of the wheel decreases rapidly. Using this procedure, longitudinal slips near to 100% can be reached.

Longitudinal μ-slip curve

Figure 15 shows the friction coefficient $\mu = F_x/F_z$ as a function of slip during braking calculated using the 1D tire model. The car velocity $v_{car} = 16.6$ m/s. The calculated friction coefficient is somewhat higher than that found in the experiment. This may be due to inaccuracy in the surface roughness power spectrum. As pointed out under Surface Roughness Power Spectrum, we could not measure the surface roughness profile of the sandpaper at the time the tire measurements were done but only much later when the sandpaper surface most likely had a modified (reduced) height profile due to wear. To account for this

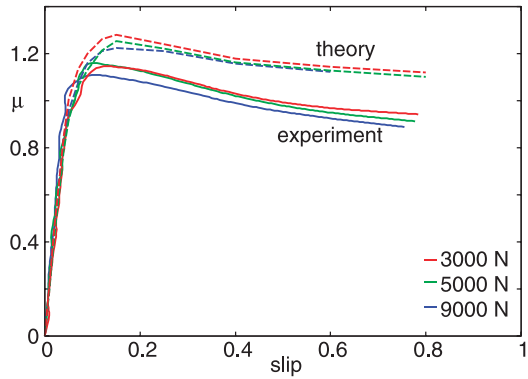

FIG. 15 — *The μ-slip curve (where* $\mu = F_x/F_N$*) for the 1D tire model compared with experimental data for the tire loads* $F_N = 3000$*, 5000, and 9000 N. The car velocity* $v_{car} = 16.6$ *m/s at* $T_0 \approx 37°C$.

effect, we somewhat arbitrarily increased the amplitude of the surface roughness by a factor of ≈1.18.

Another difference between the theory result and the experimental data is that the friction coefficient tends to decrease slightly faster with increasing slip in the measured data. We believe this may be due to a temperature effect, so far not included in the theory. (According to theory, an increase in rubber temperature decreases friction.) So far, we have included the flash temperature effect, but we do not include the fact that after some slip distance, a road-rubber macroasperity contact region may move into the "hot" strip region of rubber produced by another road asperity contact region in front of it, which is explained later in more detail. This effect, which is reducing the friction for large slip, may be the explanation why the measured friction coefficient decreases faster with increasing slip as compared to the theory.

Transverse μ-slip curve

Figure 16 shows the μ-slipangle curve, where $\mu = F_y/F_N$, for the 1D tire model compared with experimental data for the tire loads $F_N = 3000$ N (Fig. 16a), $F_N = 5000$ N (Fig. 16b), and $F_N = 9000$ N (Fig. 16c). In the calculations the background temperature T_0 has been chosen to be the same as the measured surface temperature. The tire tread surface temperature was measured at the center of the tire after rotating half a full rotation out of the footprint (see Fig. 17b), and we have taken this temperature as our background temperature. Thus T_0 depends on the slipangle and on the load. Note that the temperature variation is very large, from ≈36°C at the smallest load and slipangle zero (start of measurement) to ≈75°C at the highest load and slipangle ≈10° (and even higher temperature for the negative slipangles, which were not used in the calculations). The strong increase in the temperature during cornering results in much smaller friction coefficients compared with braking, where the

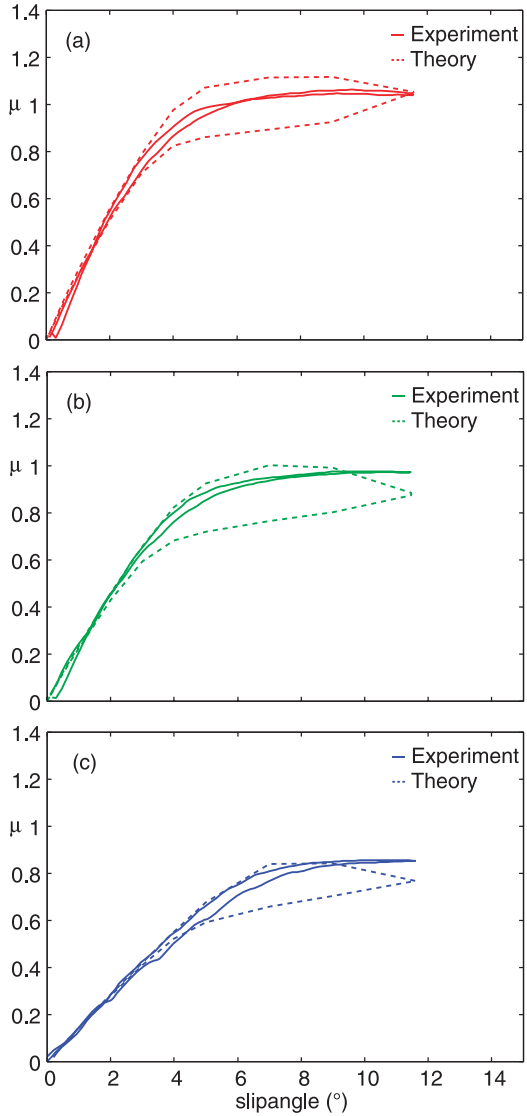

FIG. 16 — μ-*Slipangle curve (where* $\mu = F_y/F_N$*) for the 1D tire model compared with experimental data for the tire loads* $F_N = 3000$ *N (a), 5000 N (b), and 9000 N (c). The car velocity* $v_{car} = 16.6$ *m/s.*

temperature increase is much smaller (see Fig. 15). This is also illustrated in Fig. 18 that reproduces the results from Fig. 16b and also shows the calculated friction coefficient assuming the same temperature as in the calculation of the longitudinal μ-slip curve in Fig. 15.

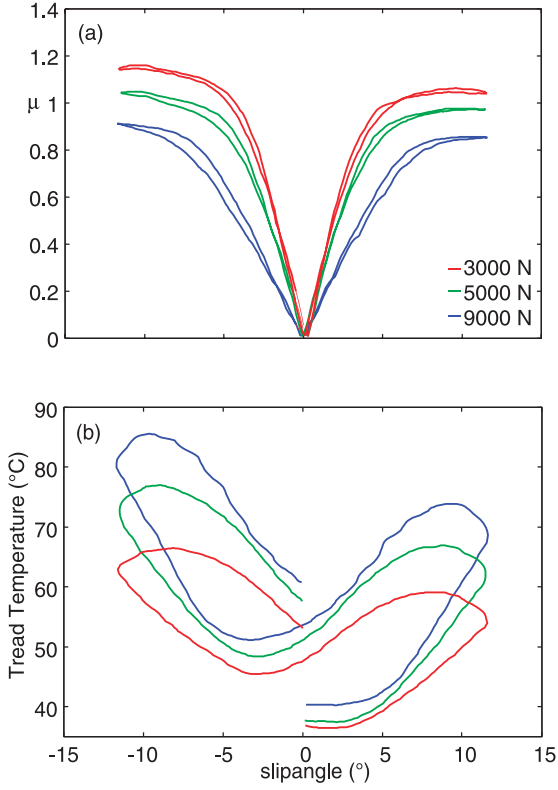

FIG. 17 — *(a) Measured μ-slipangle curves for the tire loads* $F_N = 3000$, *5000, and 9000 N. (b) Tread surface temperature was measured at a center position of the tire after half a rotation. The slipangle has been changed with ±2°/s. It was first changed from 0 to 12° then to −12° and back to 0.*

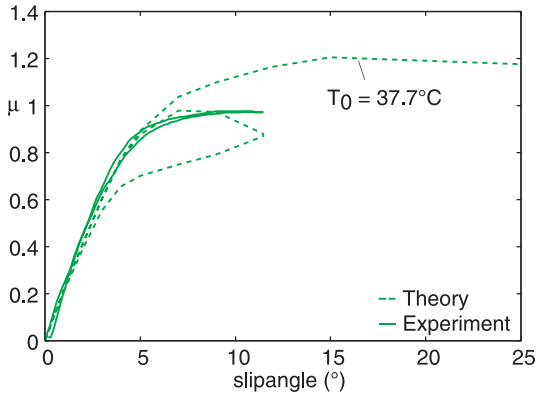

FIG. 18 — *Lateral μ-slip curve for the 1D model compared with the experimental results for the tire load* $F_N = 5000$ *N. In the upper curve, the background temperature was fixed at 37.7°C. In the lower curve, the background temperature varied between 30 and 70°C (from Fig. 17b).*

The background temperature in the study mentioned above may differ from the actual background temperature for the following reasons. First, it is the measured surface temperature; surface temperature may differ from the temperature inside the rubber (in the surface region), the relevant temperature for rubber friction. In addition, it is the temperature at one spot on the tire and it may differ from that of other surface areas, depending on where most of the friction energy is produced, which depends on the tire-road footprint pressure distribution and hence on the tire load. Finally, it is the temperature after half a tire rotation, whereas the relevant temperature is the temperature after one tire rotation, i.e., just when a tread block enters the contact region again.

The calculated results in Fig. 16 exhibit a stronger variation with the load than found in the experiment. Also, the hysteresis between increasing and decreasing slipangle is larger in the theory predictions than in the observations in the experiments. In theory, the hysteresis is entirely due to the change in background temperature. Thus, the difference between theory and experiment may reflect uncertainty in $T_0(t)$ as discussed above. However, there may be another effect related to rubber wear and contamination of the road track (see *Discussion*).

Discussion

Figure 17 shows the measured μ-slipangle curves for the tire loads $F_N = 3000$, $F_N = 5000$, and $F_N = 9000$ N. In the experiment, the slipangle has been changed by 2° (or −2°) per second. It was first changed from 0 to +12°, then to −12°, and then back to 0°. During this cycle, the tire temperature varies as shown in Fig. 17b, where we show the tire tread surface temperature measured in the center of the tire after half a tire rotation. Note that, as expected, the tire temperature is higher for negative slipangles than for positive slipangles due to increased time of frictional heating (the cornering angle first goes positive and then negative). One remarkable effect is that the rubber-road friction is larger for negative slipangles as for positive slipangles in spite of the higher temperature for negative slipangles. We believe that this effect, and the reason for why the hysteresis in the friction is larger in the calculations compared with the experiments, may be due to contamination of the road surface by hot rubber fragments (smear) that may continuously increase the contribution to the friction from the area of real contact. This effect is known to occur on Formula 1 race tracks, but it may also occur in these indoor experiments due to high temperatures and severe wear. In addition, the tire body is asymmetric, which could contribute to the difference between positive and negative slipangles.

2D Tire Model

The inputs for the 2D tire model are the tire load, tire rolling velocity, and tire (or car) center of mass velocity as well as the camber and cornering angles.

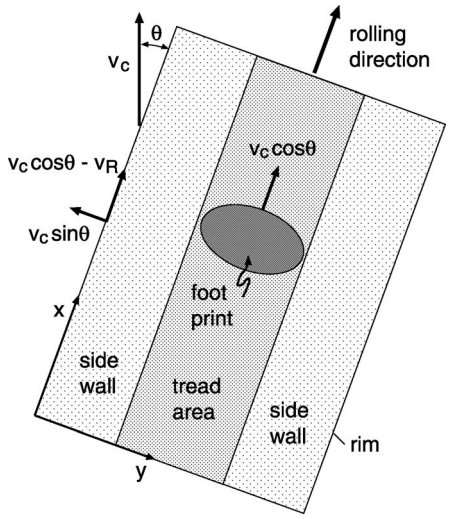

FIG. 19 — *2D model of a tire (schematic). The car velocity* υ_c *points in another direction than the rolling direction, resulting in a nonzero cornering angle* θ.

We also need in general the tire mass and moment of inertia. For tire dynamics, we need the longitudinal and transverse tire stiffness and the lowest longitudinal and transverse tire vibration frequency and damping. The outputs are all the forces and moments acting on the tire. We note that cambering is included in our 2D tire model in the same way as it is usually included in the 1D brush model by assuming that the tire rim is curved. That is, the cambering force results when a point on the outer surface of a leaned and rotating tire that would normally follow a path that is elliptical when projected onto the ground is forced (due to friction) to follow a straight path while coming in contact with the ground. For the friction law, we need the surface roughness power spectrum, the tread viscoelastic modulus, the tread heat conductivity, capacity, and the tread mass density. Slip velocities result from solving the full set of equations of motion and cannot be determined a priori. Slip ratios are defined in the usual (standard) way described in the literature and are briefly discussed below.

The tire model is shown schematically in Fig. 19. A coordinate system with the y axis in the transverse direction and the x axis along the longitudinal rolling direction is introduced. The road is considered as stationary. The car velocity $v_c(t)$, the rolling velocity $v_R(t)$, and the cornering angle $\theta(t)$ determine the transverse $v_y(t)$ and longitudinal $v_x(t)$ velocities of the rim:

$$v_y = v_c \sin\theta,$$

$$v_x = v_c \cos\theta - v_R.$$

The longitudinal slip $s(t)$ is determined by

$$s = \frac{v_x}{v_c \cos\theta} = \frac{v_c \cos\theta - v_R}{v_c \cos\theta}.$$

When the cornering angle $\theta = 0$, the equation simplifies to

$$s = \frac{v_c - v_R}{v_c}.$$

The slip $s(t)$ and the cornering angle $\theta(t)$ depend on the time t for nonstationary tire dynamics. The footprint moves in the rolling direction with the rolling velocity $v_c \cos\theta - v_x = v_R$ relative to the rim and with the velocity $v_c \cos\theta$ relative to the road.

The tire body is described as a set of mass points connected with viscoelastic springs with the elasticity k and the viscous damping γ. The springs have both elongation and bending elasticity. They are denoted by k and $k_B = k'$, and the corresponding viscous damping coefficients γ and $\gamma_B = \gamma'$. There are N_x and N_y tire-body blocks assumed along the x and y directions with $\mathbf{x}_{ij} = (x_{ij}, y_{ij})$ denoting the displacement vector of the tire-body block (i, j) $(i = 1,...,N_x, j = 1,...,N_y)$. As the tire is a torus shaped object, we use periodic boundary conditions in the x direction so that $x_{N_x+1,j} = x_{1,j}$ and $y_{N_x+1,j} = y_{1,j}$
The following boundary conditions apply. For $i = 0,\ldots, N_x + 1$:

$$\dot{y}_{i0} = v_y, \quad \dot{x}_{i0} = v_x,$$

$$\dot{y}_{i,N_y+1} = v_y, \quad \dot{x}_{i,N_y+1} = v_x.$$

For stationary tire motion, these equations can be reduced to

$$y_{i0} = v_y t, \quad x_{i0} = v_x t,$$

$$y_{i,N_y+1} = v_y t, \quad x_{i,N_y+1} = v_x t.$$

For $j = 1,...,N_y$, the periodic boundary conditions are

$$y_{N_x+1,j} = y_{1j}, \quad x_{N_x+1,j} = x_{1j},$$

$$y_{0j} = y_{N_x,j}, \quad x_{0j} = x_{N_x,j}.$$

If the mass of a tire-body element (i, j) is denoted by m_j, we obtain for $i = 1,...,N_x$, $j = 1,...,N_y$ as follows:

$$\begin{aligned} m_j \ddot{y}_{ij} = {} & F_{yij} + k_{yj}(y_{i,j-1,} - y_{ij}) + k_{yj+1}(y_{i,j+1} - y_{ij}) + \gamma_{yj}(\dot{y}_{i,j-1} - \dot{y}_{ij}) \\ & + \gamma_{yj+1}(\dot{y}_{i,j+1} - \dot{y}_{ij}) + k'_{xj}(y_{i+1,j} + y_{i-1,j} - 2y_{ij}) \\ & + \gamma'_{xj}(\dot{y}_{i+1,j} + \dot{y}_{i-1,j} - 2\dot{y}_{ij}), \end{aligned}$$

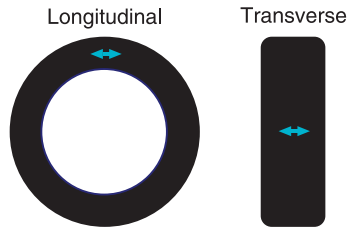

FIG. 20 — *Longitudinal and transverse tire vibrational modes of an unloaded tire with fixed rim.*

$$\begin{aligned} m_j\ddot{x}_{ij} = {} & F_{xij} + k_{xj}(x_{i-1,j} - x_{ij}) + k_{xj}(x_{i+1,j} - x_{ij}) + \gamma_{xj}(\dot{x}_{i-1,j} - \dot{x}_{ij}) \\ & + \gamma_{xj}(\dot{x}_{i+1,j} - \dot{x}_{ij}) + k'_{yj}(x_{i,j-1} - x_{ij}) + k'_{yj+1}(x_{i,j+1} - x_{ij}) \\ & + \gamma'_{yj}(\dot{x}_{i,j-1} - \dot{x}_{ij}) + \gamma'_{yj+1}(\dot{x}_{i,j+1} - \dot{x}_{ij}). \end{aligned}$$

In the equations above, F_{xij} and F_{yij} are the force components in the x and y directions. They are acting on the tire-body block (i, j) from the tread block (i, j). Therefore, $\mathbf{F}_{ij} = (\mathrm{F}_{xij}, F_{yij})$ is only nonzero when (i, j) is in the tire tread area. The viscoelastic properties of the tire body are determined by 16 parameters, namely, the tire-body viscoelastic spring parameters (k, γ) and (k', γ') in the tread area and in the sidewall area. These parameters must be optimized to reproduce a number of measured tire properties, e.g., the longitudinal and transverse tire stiffness values for three different loads and also the frequency and damping of the lowest longitudinal and transverse tire vibrational modes. The vibrational modes are shown in Fig. 20. The optimization is performed by using the amoeba method of multidimensional minimization [*24*].

Tire Body Optimization

As discussed above, there are 16 unknown parameters that need to be determined. In our tire-body optimization, 10 of these parameters were deduced from experimental data, whereas six parameters are imposed to get all quantities defined. If Q denotes the ratio of the width of the tire-body sidewall block and the width of the tire-body tread area block, then these conditions are as follows:

On the sidewall,

$$\gamma_x = \gamma_y Q^2, \quad \gamma'_x = \gamma'_y Q^2.$$

In the tread area,

$$\gamma_y = 2\gamma_y(1)Q, \quad \gamma'_x = 2\gamma'_x(1)/Q,$$

$$\gamma'_y = 2\gamma'_y(1)Q, \quad \gamma_x = 2\gamma_x(1)/Q,$$

where $\gamma_y(1)$, $\gamma'_y(1)$, $\gamma_x(1)$, and $\gamma'_x(1)$ all refer to the sidewall. Note that γ_y and γ'_y are fitted to agree with the damping constant of the tire transverse and longitudinal vibration modes. The factor of 2 in the equations above is quite arbitrary, but reflects an expected larger damping of the tire body in the tread area.

The tire optimization is done in an iterative way. We first use the measured tire vibration frequencies and damping constants to determine the tire-body spring constants and damping in a similar way as for the 1D tire. That is, for all tire-body spring and damping constants (on both sidewall and tread area) during the iteration, we replace

(a) for transverse mode,

$$k_y \rightarrow k_y \times (\omega_{\mathrm{T}}/\omega_{\mathrm{Tc}})^2, \quad \gamma_y = \gamma_y \times (\gamma_{\mathrm{T}}/\gamma_{\mathrm{Tc}}),$$

(b) for longitudinal mode,

$$k'_y \rightarrow k'_y \times (\omega_{\mathrm{L}}/\omega_{\mathrm{Lc}})^2, \quad \gamma'_y = \gamma'_y \times (\gamma_{\mathrm{L}}/\gamma_{\mathrm{Lc}}).$$

We iterate until the measured tire vibration frequencies ω_T and ω_L and damping γ_T and γ_L are reproduced.

Next, the tire longitudinal and transverse stiffness values for three loads (total of six parameters) are used. For transverse stiffness, in the tread area, k_y and k'_x and also in the sidewall k'_x are varied. For longitudinal stiffness, in the tread area k'_y and k_x and also in the sidewall k_x are varied.

The optimization of the transverse and longitudinal tire stiffness for all three tire loads is performed using the amoeba method to minimize the effective potential or error functions:

$$V_T = \left[\sum \left(\frac{C_{\mathrm{T}}}{C_{\mathrm{Tc}}} - 1 \right)^2 \right]^{1/2},$$

$$V_L = \left[\sum \left(\frac{C_{\mathrm{L}}}{C_{\mathrm{Lc}}} - 1 \right)^2 \right]^{1/2},$$

where C_{T} is the measured tire stiffness and C_{Tc} the calculated (for a given set of spring constants k and damping γ) transverse stiffness value, and similar for the longitudinal stiffness C_{L} and C_{Lc}. The tire stiffness values are defined as $C_{\mathrm{T}} = F_{\mathrm{y}}/(\theta\, F_{\mathrm{N}})$ (where θ is in degrees) as the slipangle $\theta \rightarrow 0$ and $C_{\mathrm{L}} = F_x/(sF_{\mathrm{N}})$ as the slip $s \rightarrow 0$. The sum Σ is over the three different tire loads. In Tables 1 and 2, we show the results of a tire optimization. The longitudinal and transverse tire vibrations and damping are perfectly reproduced. The transverse (cornering) stiffness is also very well reproduced. However, the longitudinal stiffness for the largest load shows some discrepancy. Table 3 also presents several other

TABLE 1 — *Calculated (optimized) and experimental values for the longitudinal and transverse tire vibration eigenfrequencies and dampings.*

	ω_T (Hz)	γ_T (s^{-1})	ω_L (Hz)	γ_L (s^{-1})
Calculated	46.1	1.08	63.0	2.72
Experimental	46.2	1.10	63.0	2.72

calculated quantities for which no measured values were known to us. The pneumatic trail is defined as M_z/F_y, and the self-aligning moment stiffness is defined as $M_z/(\theta\ F_N)$ as the slipangle $\theta \to 0$. Finally, the camber stiffness coefficient is defined as $F_y/(\phi\ F_N)$ as the camber angle (in degree) $\phi \to 0$. For the loads $F_N = 3000$, 5000, and 9000 N the length of the tire footprint is $L_x = 90$, 128, and 189 mm, respectively. Thus, the ratio between the pneumatic trail δ (see Table 3) and the length of the footprint are $\delta/L_x = 0.21$, 0.27, and 0.28, respectively. The simple brush model predicts $\delta/L_x = 1/6 \approx 0.17$, but it is known from measurements that the pneumatic trail usually is larger than predicted by the brush model, in accordance with our model predictions.

The tire-body elasticity and damping for square tire-body elements as resulted from the tire optimization are shown in Tables 4 and 5. Note that the sidewall spring constants k_y and k_{By} are considerably softer than the other spring constants. We show in *Numerical Results* that these spring constants are determined mainly by the inflation pressure. Note also that, as expected, the spring constants of the tire body in the tread area are higher than in the sidewalls.

Consider a rubber block with thickness d and the width and height b. If the stress $\sigma = F/bd$ is applied to two opposite sides, it will elongate a distance u so the strain $\varepsilon = u/b$ (see Fig. 21). If E is the elastic modulus, we have $\sigma = E\varepsilon$, which gives $F = uEd$ or the elongation spring constant $k = Ed$. Similar the shear spring constant $k_B = Gd$, where $G = E/(2(1 + v))$, is the shear modulus. If the thickness of the rubber block $d = 1$ cm as typical for tire body and if $E = 10$ MPa as is typical for the low-frequency Young's modulus of filled rubber, we get $k = 100$ kNm and $k_B \approx 30$ kNm. These values are similar but slightly smaller than the values given in Table 4. This is expected, as in the tire body are fibers with much higher stiffness than the rubber itself. Note, as pointed out above, that the sidewall spring constants k_y and k_{By} are considerably softer than the other spring constants and

TABLE 2 — *Calculated (optimized) and experimental values for the longitudinal and transverse stiffnesses for the three different normal loads.*

F_N (N)	C_T	C_{Tc}	C_L	C_{Lc}
3000	0.31	0.30	25.0	26.3
5000	0.23	0.21	22.5	21.5
9000	0.14	0.14	20.0	16.2

TABLE 3 — *Values for the pneumatic trail, the self-aligning moment stiffness coefficient, and the camber stiffness coefficient after the tire optimization for the three different normal loads.*

F_N (N)	Pneumatic trail (mm)	Self-aligning moment stiffness coefficient	Camber stiffness coefficient
3000	18.9	0.0057	0.0094
5000	34.2	0.0071	0.0093
9000	53.3	0.0077	0.0112

also smaller than estimated above for a rubber block. The reason is that in our model, these two spring constants have a geometrical origin in combination with the inflation pressure [see *Influence of tire gas (inflation) pressure*].

We have performed a calculation of the tire-body longitudinal and transverse stiffness, neglecting the deformations of the tread blocks. In this case, the tire stiffness values are entirely due to the deformations of the tire body. We find that neglecting the deformations of the tread blocks increase the tire longitudinal stiffness by ≈18% and the transverse tire stiffness by ≈8%.

In addition to the longitudinal and transverse tire stiffness obtained from the μ-slip and μ-cornering-angle curves, we have also measured the longitudinal (K_L) and transverse (K_T) stiffness defined as follows. The tire is pushed against a substrate with a given load, and a tangential force F is applied while the tangential tire displacement u from the center axis is measured. The tire is not allowed to rotate. In this way, we obtain a $u(F)$ curve that is nearly linear up to the point when the tire starts to slip. We define $K_L = F_x/u_x$ and $K_T = F_y/u_y$. In Fig. 22, we show the measured and calculated relation between F_x/F_N and the longitudinal displacement, and in Fig. 23 the same data for transverse tire displacement are shown. In Fig. 24, we show the calculated results for K_L and K_T for three different loads and the measured data for two loads. Although the trend in the data as a function of the normal load are the same, there are some quantitative differences. The calculated stiffness values are higher than measured. The origin of this may reflect uncertainties in the experimental data used in the optimization of the tire body, in particular, in the tire resonance frequencies (and damping) ω_T and ω_L, which were not measured directly but deduced from other experimental data.

Tire Footprint Pressure Distribution

In the tire dynamics calculations, we use the measured tire footprint pressure distribution shown in Fig. 25 for the normal loads (Fig. 25a) $F_N = 3000$ N, (Fig.

TABLE 4 — *Calculated (optimized) tire-body spring constants.*

Location	k_x (kN/m)	k_{Bx} (kN/m)	k_y (kN/m)	k_{By} (kN/m)
Sidewall	141.1	68.0	11.6	22.5
Tread area	223.4	102.4	105.6	56.6

TABLE 5 — *Calculated (optimized) tire-body damping constants.*

Location	γ_x (Ns/m)	γ_{Bx} (Ns/m)	γ_y (Ns/m)	γ_{By} (Ns/m)
Sidewall	0.736	2.015	0.700	2.088
Tread area	1.472	4.030	1.400	4.175

25b) $F_N = 5000$ N, and (Fig. 25c) $F_N = 9000$ N. Our tire model does not use the exact tread pattern from the real tire, but assumes square tread blocks. The pressure profiles shown in Fig. 25 are processed so that the tread blocks experience contact pressures with a very similar spatial distribution as the measured footprint pressure distribution. Also note that the pressure profiles in Fig. 25 refer to a static condition. During rolling, braking, and cornering, the pressure distribution will be modified, but this effect is not taken into account in the present study.

Numerical Results

In this section, we first compare the μ-slip curves calculated with the 2D tire model with those of the 1D tire model. We also compare the calculated self-aligning moment curve with the experimental data. We present snapshots of the tire deformation field during braking and cornering. Finally, we study the influence of the tire inflation pressure on the μ-slip and μ-slipangle curves.

Comparison with the 1D-tire Model

In Fig. 26, we compare the longitudinal μ-slip curve for the 1D and 2D tire models, and the experimental results for the tire load $F_N = 5000$ N. Note that the 1D and 2D tire models give very similar results.

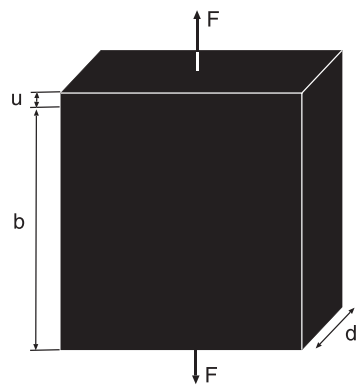

FIG. 21 — *Rubber block sheet of square form (side* b*) and thickness* d *exposed to a uniform stress* σ = F/db *will elongate a distance* u.

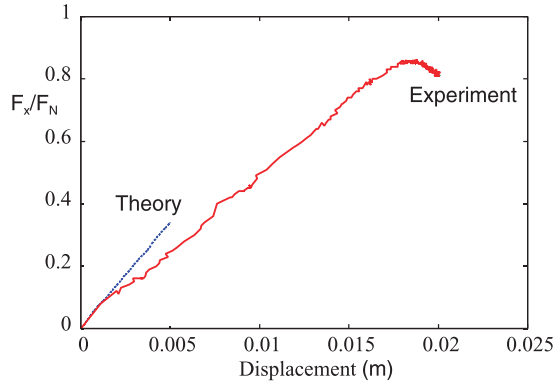

FIG. 22 — *Calculated and experimental results for the longitudinal stiffness* K_L *for the tire load* F_N *= 5000 N and drive velocity* $\upsilon = 2.2$ *mm/s.*

Self-Aligning Torque: Comparison with Experimental Data

Figure 27 shows the self-aligning moment as a function of the slipangle for the tire loads $F_N = 3000$ N, $F_N = 5000$ N, and $F_N = 9000$ N. The measured result is given by the solid line and the prediction of the 2D tire model by the dashed line. Note that the maximum of the measured self-aligning moment is larger than predicted theoretically. This may be due to the modifications of the footprint pressure profile during cornering (in the calculations the static measured footprints are always used).

Relaxation Length

Figure 28 shows the variation of the transverse force on the tire (in units of the normal force F_N) as a function of time when the cornering angle increases

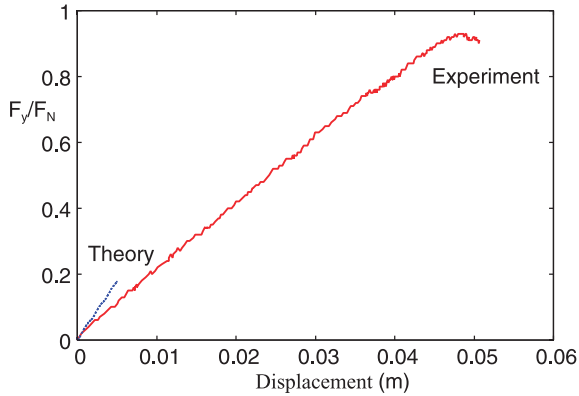

FIG. 23 — *Calculated and experimental results for the lateral stiffness* K_T *for the tire load* $F_N =$ *5000 N and drive velocity* $\upsilon = 6.45$ *mm/s.*

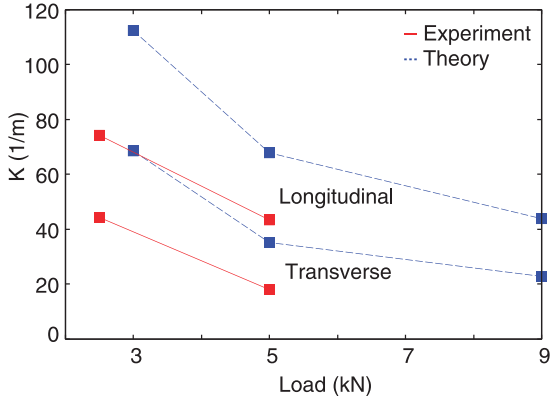

FIG. 24 — *Calculated results for the stiffness parameters* K_L *and* K_T *for three different loads and the corresponding measured data for two loads.*

linear with time from $\theta_0 = 0°$ at time $t_0 = 0$ to $\theta_1 = 1$, 3, 7, and 12° at $t_1 = 0.02$ s. The relaxation length L is the tire rotation distance for the transverse force to reach 60% of its final value. In the present case, we get $L \approx 0.5$ m for $\theta_1 = 1$ and 3°. This corresponds to approximately one-fourth of a full tire rotation. For large slipangles, the relaxation length is smaller, as also observed in experiments.

Tire Body Deformation Field

Figure 29 shows snapshots of the tire deformation field during braking and Figure 30 shows snapshots during cornering.

Influence of Tire Gas (Inflation) Pressure

The inflation pressure has two (related) influences on the tire dynamics: increasing the inflation pressure will (1) increase the tire body stiffness that will in turn increase the longitudinal and transverse (cornering) tire stiffness, and (2) will reduce the length of the tire footprint that will in turn reduce the longitudinal and transverse (cornering) tire stiffness. For vehicle tires, these two effects may nearly cancel each other, often resulting in only a small change in the tire stiffness that could be of either positive or negative sign, depending on which effect is stronger.

In a first approximation, the normal pressure in the footprint is given by the inflation pressure (this would hold exactly for a membrane without bending stiffness) and the area of the footprint would be proportional to the inflation pressure. In this case, if both the width and the length of the footprint would change with an equal factor, then the length $L_x \sim p^{1/2}$. If the width would instead be constant (as it must be the case for small inflation pressures or large tire loads), then $L_x \sim p$.

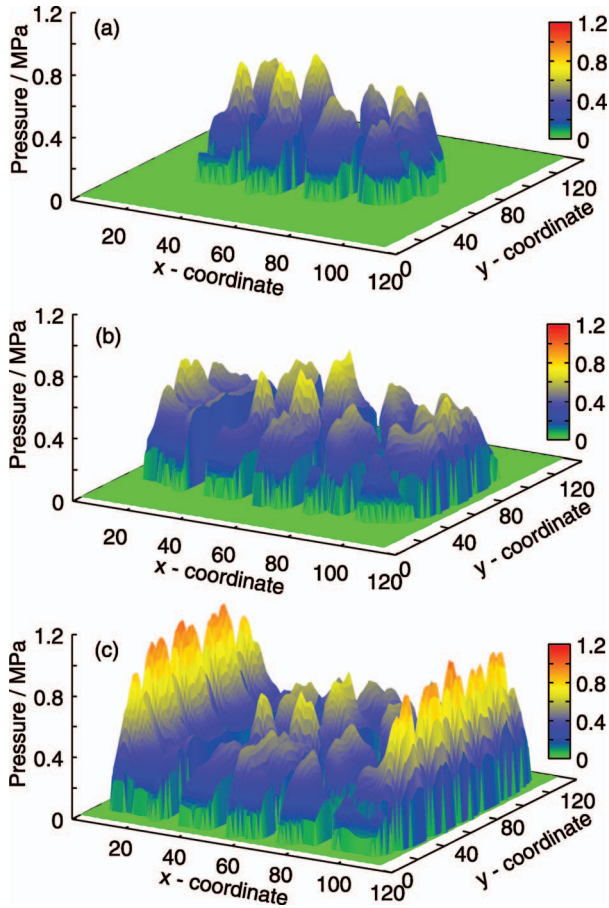

FIG. 25 — *Tire footprints pressure distribution for the normal loads* $F_N = 3000$ *N (a), 5000 N (b), and 9000 N (c).*

Increasing the inflation pressure will result in a stiffening of the tire sidewalls that can be understood as follows. Assume for simplicity that the tire cross section is rectangular with the tread area of width w, and the sidewall of width h (see Fig. 31). When we apply a transverse force uniformly on the tread area, the tire body deforms in a manner that we assume is as indicated in Fig. 31. This will in first approximation change the volume of the gas contained in the tire by $\Delta V = Lwh - Lwh \cos \alpha \approx Lwh\alpha^2/2$, resulting in a work done against the gas pressure by $p\Delta V$. In our tire model, we do not account for the inflation pressure explicitly, so this effect of the gas in the tire must be contained in the tire springs used in our model (see 2D Tire Model). In our 2D tire model, the tire body is discretized into square blocks of length and width a in the tread

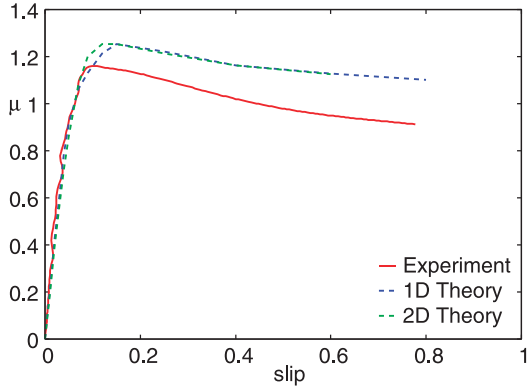

FIG. 26 — *Longitudinal* μ*-slip curve for the 1D and 2D models compared with the experimental results for the tire load* $F_N = 5000$ *N.*

area, and into rectangular blocks on the sidewalls with length $b_x = a$ and width b_y. Thus, if there are N_y blocks in the y direction, $N_y b_y = h$, and if L is the length (x direction) of the 2D tire, then $N_x b_x = L$. The transverse tire deformations involve only the sidewall springs k_y. In our model, the deformation in Fig. 31 moves the tread area relative to the (fixed) rim in the transverse direction by the amount $h\sin\alpha \approx h\alpha$ so that each spring will elongate (on one side) or contract (on the other side) with $b_y\alpha$. If the total number of side wall springs k_y is denoted by $N = 2N_xN_y$, then we get the energy conservation equation:

$$\frac{1}{2}Nk_y(b_y\alpha)^2 = \frac{1}{2}Nk_y^0(b_y\alpha)^2 + p\Delta V,$$

where k_y^0 is the tire k_y spring constant for zero inflation pressure. Thus, we get

$$k_y = k_y^0 + pLwh/(2N_xN_yb_y^2),$$

or

$$k_y = k_y^0 + (pw/2)(b_x/b_y).$$

Applying instead a uniform longitudinal force on the tread area, and using the same arguments as above, one can show that

$$k_{By} = k_{By}^0 + (pw/2)(b_x/b_y).$$

Thus, one expects k_y and k_{By} to depend linearly on the inflation pressure. However, the prefactor will not be exactly $(w/2)(b_x/b_y)$ because the undeformed tire body will not be exactly rectangular as assumed above, and the deformed tire body will not involve just the simple shear deformation indicated in Fig. 31.

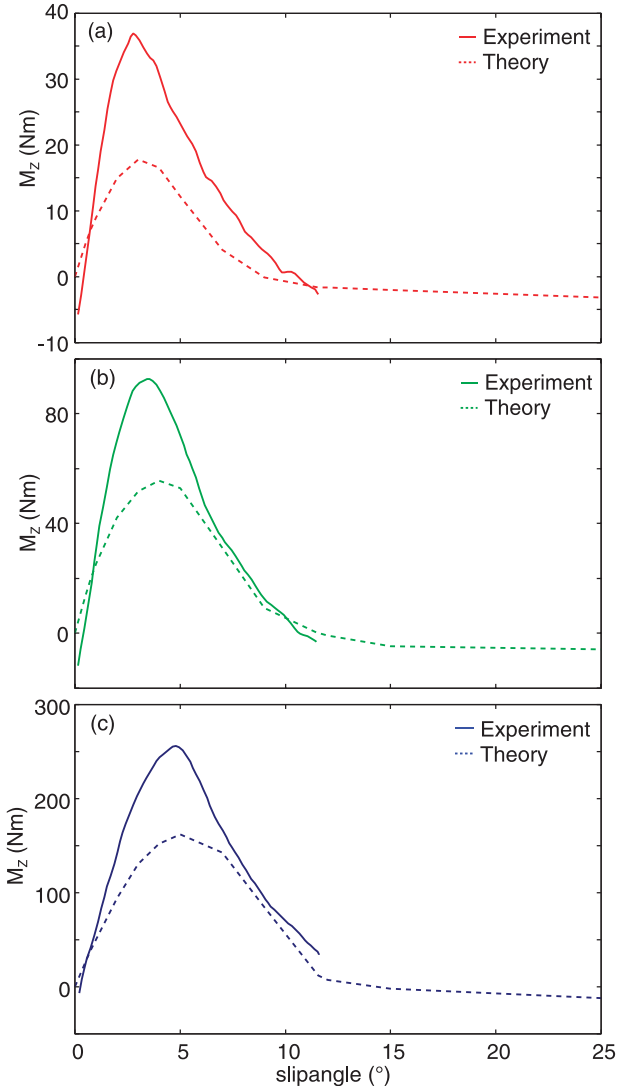

FIG. 27 — *Self-aligning moment as a function of the slipangle. The measured result is given by the solid line and the prediction of the 2D tire model by the dashed line. Tire load* $F_N = 3000$ *N (a), 5000 N (b), and 9000 N (c).*

We suppose that at nominal inflation pressure the pressure term in brackets will dominate over k_y^0 (and similar for k_{By}), and in the model calculations we will neglect the pressure-independent term. This is intuitively clear because it is much easier to displace the tread area of an uninflated tire than of an inflated tire. Note that in the present case (where $p = 0.25$ MPa, $w \approx 0.18$ m and $b_x/b_y \approx$

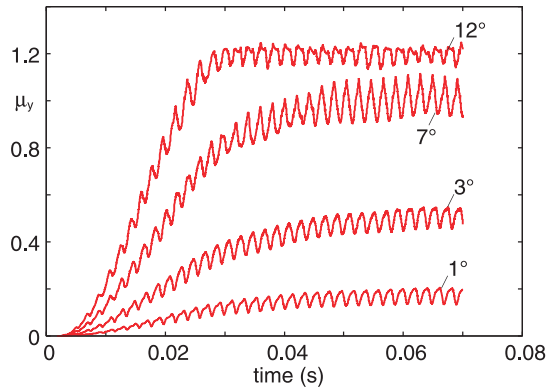

FIG. 28 — *Variation of the transverse force on the tire (in units of the normal force* F_N*) as a function of time when the cornering angle increases linear with time between* $t_0 = 0$ *s and* $t_1 = 0.02$ *s, from* $\theta_0 = 0°$ *to* $\theta_1 = 1$*, 3, 7, and 12°, for* $F_N = 5000$ *N.*

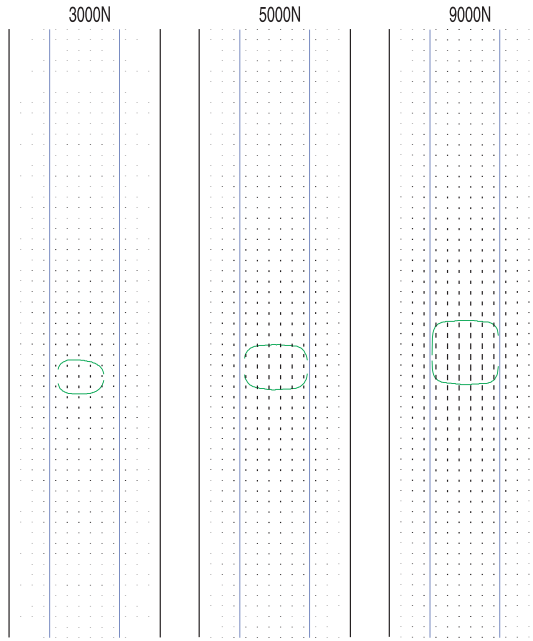

FIG. 29 — *Snapshots of the tire-body deformations for the normal load* $F_N = 3000$ *N, 5000 N, and 9000 N. In all cases, the slip* $s = 0.05$ *and the cornering angle* $\theta = 0$*. The short vertical lines indicate the displacement of the tire body from the undeformed state. The maximum tire-body displacements are 0.92, 1.39, and 1.84 cm for the tire loads* $F_N = 3000$ *N, 5000 N, and 9000 N, respectively. Rubber background temperature* $T_0 = 80°C$ *and car velocity 16.6 m/s.*

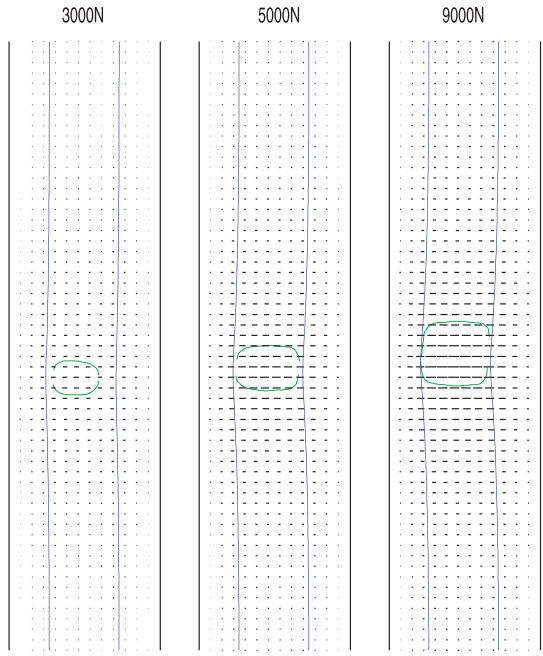

FIG. 30 — *Snapshots of the tire-body deformations for the normal load* $F_N = 3000$ *N, 5000 N, and 9000 N. In all cases, the slip* $s = 0$ *and the cornering angle* $\theta = 5°$. *The short horizontal lines indicate the displacement of the tire body from the undeformed state. The maximum tire-body displacements are 1.20, 1.81, and 2.31 cm for the tire loads* $F_N = 3000$ *N, 5000 N, and 9000 N, respectively. Rubber background temperature* $T_0 = 80°$ *C and car velocity 16.6 m/s.*

0.8), this would give a pressure contribution to k_y of $\approx 1.3 \times 10^4$ Nm and similar for k_{By}. This is remarkably close to the spring constants obtained for the optimized tire: $k_y \approx 1.0 \times 10^4$ Nm and $k_{By} \approx 1.8 \times 10^4$ Nm (see Tire Body Optimization). We also note that all the other spring constants of the optimized tire are much larger; so, in these cases, the dependency of the spring constants

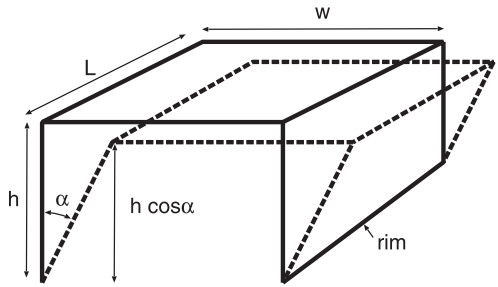

FIG. 31 — *Uniform transverse force acting on the tire tread area deforms the tire body as indicated in the figure.*

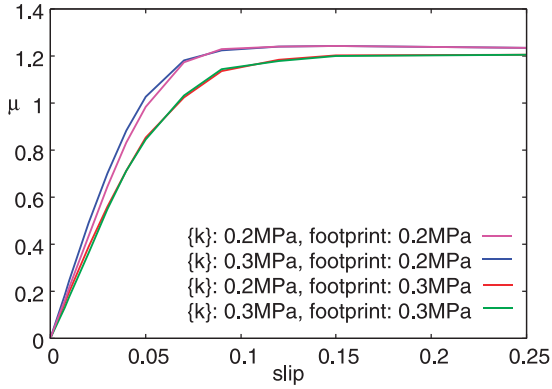

FIG. 32 — *The μ-slip curve in dependency of the tire inflation pressure. The tire body stiffness parameters {k} and the footprints have been modified to correspond to the inflation pressures 0.2 and 0.3 MPa.*

on the inflation pressure will be smaller. However, we have found that k_y and k_{By} have rather small influence on tire longitudinal and transverse stiffness (but are, of course, crucial for the longitudinal and transverse tire vibration modes), so it is still important to take into account the dependency of k_x and k_{Bx} on the inflation pressure. We expect from dimensional arguments that k_x and k_{Bx} depend on p in a similar way as k_y and k_{By}, so that

$$k_x = k_x^0 + \alpha_x(pw/2)(b_y/b_x),$$

$$k_{Bx} = k_{Bx}^0 + \alpha_{Bx}(pw/2)(b_y/b_x),$$

where we expect α_x and α_{Bx} to be of order unity. Note, from dimensional arguments that these numbers may depend on h/w. In the model calculations, we have chosen $\alpha_x = \alpha_{Bx} = 1$, but these parameters could in principle be determined by comparing how the calculated longitudinal and transverse tire stiffness compares to the measured tire stiffness for two different inflation pressures.

In Fig. 32, we show the dependency of the μ-slip curves and in Fig. 33 the dependency of the μ-slipangle curves on the inflation pressure. We have done four model calculations where the tire body stiffness parameters $\{k\}$ and the footprints have been modified to correspond to the inflation pressures 0.2 and 0.3 MPa. Note that in our model, there is a very small influence of the tire body stiffness on the μ-slip curve, whereas the μ-slip curve depends strongly on the size of the footprint. In the present calculation, the normal tire load is fixed and the footprint was taken as rectangular with equal width for the inflation pressures 0.2 and 0.3 MPa. Thus, at the lower inflation pressure the footprint is 3/2 = 1.5 times longer than at the larger inflation pressure. In reality, as the inflation pressure changes, the shape of the footprint may get

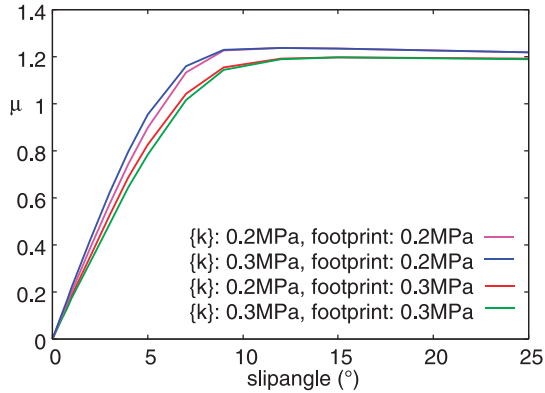

FIG. 33 — μ-*Slipangle curve in dependency of the tire inflation pressure. The tire body stiffness parameters {*k*} and the footprints have been modified to correspond to the inflation pressures 0.2 and 0.3 MPa.*

modified in a different way than assumed in our model calculations, but it is in principle easy to use footprints measured at different inflation pressures in our calculations.

Discussion

All the calculations presented above have been obtained using the 2D tire model described under 2D Tire Model, with the tire body optimized using experimental data for a passenger car tire. The viscoelastic springs associated with this tire body are kept fixed in all the calculations, except in *Numerical Results* where we study the influence of the tire inflation pressure, which affects the tension in the tire walls, on tire dynamics. Thus, the model calculations do not take into account the changes in the tire body viscoelastic properties due to variations in the tire (background) temperature. In principle, this effect can be relatively simply taken into account in the model, but has not been included so far.

We emphasize that the 2D tire model is not a "stationary tire model" but that it describes arbitrarily complex tire dynamics, e.g., combined (time-dependent) variation in the longitudinal slip, the cornering angle, and the camber angle, whereas the (forward or rolling) velocity may depend on time in any arbitrary way. We numerically solve the full (time-dependent) set of equations of motion without any limitation. In fact, even "stationary tire motion" involves non-steady tread block motion. Thus, at small slip a tread block entering the footprint is first (nearly) pinned to the substrate, and only close to the exit of the footprint will it undergo fast slip. Furthermore, after leaving the footprint the tread block may perform damped high-

frequency vibrations for a short time (resulting in high frequency noise); all this is accurately described by the tire model, although not discussed here.

In our model, the tire is discretized into blocks. To each tire-body element in the tread area, a tread block is "connected" that in turn can be discretized in the vertical direction into many (typically 10) thinner block elements (describing vertical slices of the tread block) that are coupled to each other using viscoelastic springs (determined by the measured viscoelastic modulus of the tread rubber) as described in detail in Ref. [*6*]. This model also allows a gradient in the tread rubber properties. This is typical in real applications [where a stiffer, less hysteritic rubber is often used in the upper part of the tread block to reduce (stabilize) the deformations of the tread block when exposed to large stresses, and in order to reduce the rolling resistance]. The parallel (frictional) stress that acts on a tread block is the product of the normal stress times the friction coefficient, which depends on the history of the sliding motion of the tread block element, as described by the theory of Ref. [*6*] or by the simplified friction law given by eq. 1. Thus, the present theory includes the memory effects of the friction force resulting from the nonuniform (in time) slip motion of the tread blocks.

The present study only accounts for frictional heating via the flash-temperature effect. In reality, the background temperature T_0 may also change with time, e.g., during ABS braking, or during the measurement of the μ-slip curve. It is well known in indoor measurements of tire μ-slip curves that the increase in T_0 with increasing time may result in large "hysteresis" if the slip is first increased from zero to unity, and then reduced back to zero (see [*3*]). We have not accounted this effect so far, but it can relatively easy be included in the present theory. There is also another temperature effect coming from the overlap of hot spots from different asperity contact regions that is not considered in this study (see below).

The flash temperature depends on both the slip velocity and the slip distance. The amount of dissipated energy, which is the product of friction force and slip distance, goes to zero as the slip distance goes to zero, so negligible frictional heating (and negligible temperature increase) of the rubber will occur when the slip distance is very small. In contrast, when the slip distance becomes larger than the diameter D of the macroasperity contact regions, then there is no longer any overlap between the present (say, at time t) contact region and the original (say, at time $t = 0$) macroasperity contact region, and at this point the flash temperature has been fully developed. This picture neglects the fact that after a long enough slip, a given macroasperity contact region may overlap with the "hot rubber track" emerging from another asperity contact region in front of it. Note, this hot rubber track will widen in time due to heat diffusion, and finally (for long enough time) contribute to the background temperature $T_0(t)$ (see Fig. 34). However, this effect is not important for slip up to (and slightly beyond) the point where the μ-slip curve has its maximum,

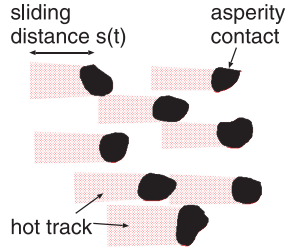

FIG. 34 — *When a rubber block slides on a rough surface, the heat produced in the asperity contact regions will result in hot tracks (dotted area) on the rubber surface. When an asperity contact region moves into the hot track resulting from another asperity contact region in front of it (in the sliding direction), it will experience a rubber temperature higher than the background temperature* T_0. *This "thermal interaction" between hot spots becomes important if the slip distance is larger than the average separation between the (macro) asperity contact regions.*

which is the most important region for practical applications (e.g., ABS braking), but it will give rise to a decrease in friction for larger slip.

ABS Braking Simulations

The theory presented may be useful to design or optimize control algorithms for ABS braking. Below, we show results using two very simple control algorithms. In both algorithms, the braking torque is changed (increased or decreased) in steps of ΔM at time $t_n = n\Delta t$ ($n = 1, 2, \ldots$). The first method assumes that the maximum friction, and the corresponding slip s^*, are both known and time independent. Thus, the braking torque is increased if the slip $s(t_n)$ at time t_n is below s^* and otherwise it is decreased (see Fig. 35). One problem here is that the slip s^* depends on the car velocity, which changes

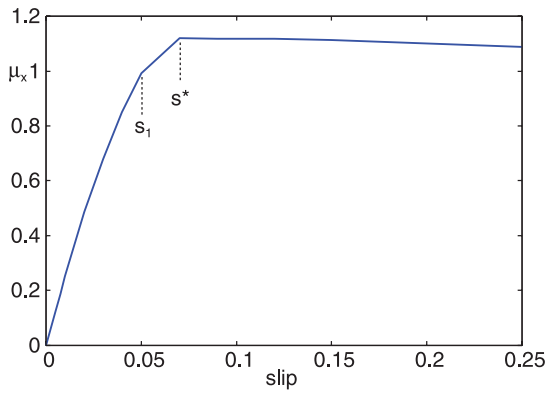

FIG. 35 — μ-*Slip curve for car velocity* $v_c = 27$ *m/s. The maximum of the* μ-*slip curve occurs for the slip* $s = s^* = 0.07$. *The ABS control algorithm should increase the braking torque when* $s < s^*$ *and reduce the braking torque when* $s > s^*$.

during the braking process. However, for the studied system $s^* \approx 0.07$ is nearly independent of the car velocity for 10 m/s $< v_c <$ 27 m/s. Note that s^* depends on the background temperature T_0 that increases during braking due to frictional heating. However, in the present study we neglect this effect.

For the second control algorithm **b**, we assume that s^* is unknown. However, by analyzing the variation with time of the longitudinal friction $F_x(t)$ and the slip $s(t)$, one can determine whether being on the ascending or descending side of the maximum s^*. Thus, if

$$F_x(t_n) > F_x(t_{n-1}) \quad \text{and} \quad s(t_n) < s(t_{n-1}),$$

or if

$$F_x(t_n) < F_x(t_{n-1}) \quad \text{and} \quad s(t_n) > s(t_{n-1}),$$

implies $s(t_n) > s^*$, in which case the braking torque at time t_n must be decreased, otherwise increased. Here, $F_x(t_n)$ is the longitudinal friction force and $s(t_n)$ the slip at time $t_n = n\Delta t$ ($n = 1, 2, \ldots$).

We now present numerical results to illustrate the two ABS braking algorithms. Let M denote the mass-load acting on a wheel and I the moment of inertia of the wheel *without* the tire. For simplification purposes, the suspension is rigid and mass-load transfer is neglected. The motion equation for the center of mass coordinate $x(t)$ of the wheel and the angular rotation coordinate ϕ (t) are as follows:

$$Mx = F_{\text{rim}}, \tag{2}$$

$$I\phi = M_{\text{rim}} - M_{\text{B}}, \tag{3}$$

where F_{rim} is the force acting on the rim, M_{B} is the braking torque, and M_{rim} the torque acting on the rim from the tire. For constant rolling velocity, $F_{\text{rim}} = F_{\text{f}}$ is the tire-road friction force and $M_{\text{rim}} = RF_{\text{f}}$, where R is the rolling radius. But during angular accelerations, these relations are no longer true because of tire inertia effects. We have used $M = 360$ kg and $\text{I} = 0.4$ kgm^2 in the calculations.

First, we investigate control algorithm **a**. We assume $\Delta M = 200$ Nm, $\Delta t =$ 0.03 s, and $s^* \approx 0.05$ (compare Fig. 35). The actual maximum of the μ-slip curve occurs for $s^* = 0.07$, and we discuss below the difference between using these two different values for s^*. Figure 36 shows the car velocity v_c and the rolling velocity v_R (Fig. 36a), the longitudinal slip (Fig. 36b), and the braking torque (Fig. 36c) shown as a function of time. The duration ($t \approx 2$ s) to reduce the car velocity from $v_0 = 27$ m/s to $v_1 = 10$ m/s corresponds to an effective friction coefficient $\mu = (v_0 - v_1)/gt = 0.87$, which is smaller than the actual maximum of the μ-slip curve. The slope of the car-velocity line in Fig. 36a for $t > 0.2$ s corresponds to the friction coefficient 0.92. This is larger than the average friction calculated from the stopping time. The slightly smaller friction

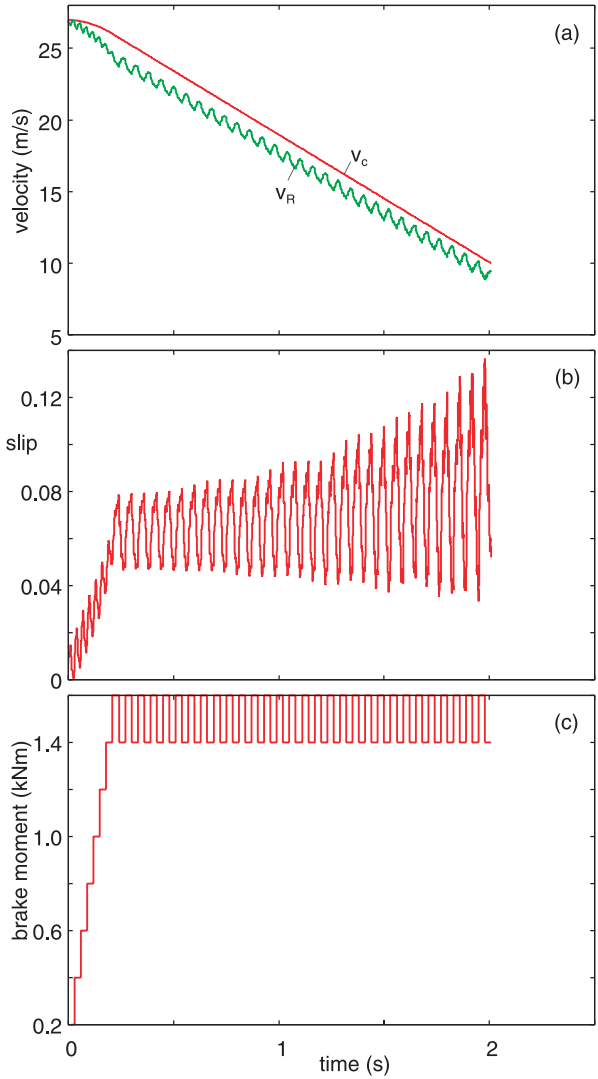

FIG. 36 — *(a) Car velocity* v_c *and the rolling velocity* v_R *as a function of time* t. *The slip (b) and the braking moment (c) as a function of time* t. *For ABS braking, using algorithms* ***a*** *(see text for details).*

obtained from the stopping time reflects the short initial time interval, which is necessary to build up the braking torque.

In Fig. 37, we show results for the second ABS control algorithm. Note that here it also takes about 2 s to reduce the car velocity from $v_0 = 27$ m/s to $v_1 = 10$ m/s, which gives the same effective friction as obtained using the first ABS control algorithm. The maximum in the μ-slip curve (see Fig. 35) depends on

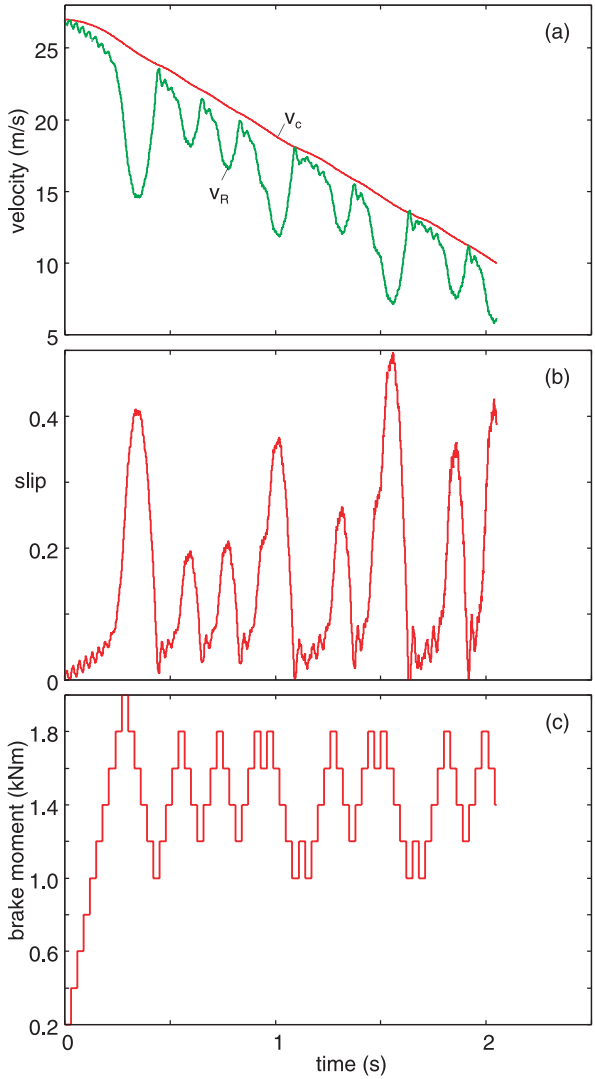

FIG. 37 — *(a) Car velocity* v_c *and the rolling velocity* v_R *as a function of time* t. *The slip (b) and the braking moment (c) as a function of time* t. *For ABS braking, using algorithms* ***b*** *(see text for details).*

the car velocity and is of order $\mu_{max} = 1.1$, meaning that the ABS braking control algorithm used above could still be improved. Note also that the wheel tends to lock about three or four times per second. Because the speed of the car is usually not known during ABS braking, the control algorithms used in most cars today determine the braking torque only from the wheel rotation acceleration. This is possible because, as the wheel tends to lock, the rotational

velocity decreases very rapidly, and hence the ABS controller decreases the braking torque.

Note that the (average) of the slip in Figs. 36b and 37b increases with increasing time or, equivalently, with decreasing car velocity. This is due to the fact that the time it takes for the wheel to lock, when the slip $s > s^*$, decreases as v_c decreases. Thus, during the time period Δt between two changes of the brake torque, the maximum slip (corresponding to the minimum rolling velocity) will increase as v_c decreases. This is easy to show mathematically. Because the car velocity changes slowly compared to the rolling velocity, from the definition $s = (v_c - v_R)/v_c$ we get

$$\frac{dv_R}{dt} \approx -v_c \frac{ds}{dt}.$$

If we approximate the μ-slip curve for $s > s^*$ with a straight line,

$$\mu_{eff} \approx \mu_0 - \Delta\mu s,$$

we get from (3)

$$I\frac{d^2\phi}{dt^2} = \frac{I}{R}\frac{dv_R}{dt} \approx -\frac{Iv_c}{R}\frac{ds}{dt} = MgR[\mu_0 - \Delta\mu s] - M_B,$$

or

$$\frac{ds}{dt} = -A + Bs,$$

where $A = (MgR\ \mu_0 - M_B)(R/Iv_c)$ and $B = \Delta\mu\ (MgR^2/Iv_c)$. Because A and B can be considered as constant during the time interval between the changes in the braking torque, we get

$$s(t) = \left(s(0) - \frac{A}{B}\right)e^{Bt} + \frac{A}{B},$$

where

$$\frac{A}{B} = \frac{1}{\Delta\mu}\left(\mu_0 - \frac{M_B}{MgR}\right).$$

One can show that

$$s(0) - \frac{A}{B} = \left[s(0) - s^*\right] + \frac{M_B - M_B^*}{\Delta\mu MgR},$$

where $M_B^* = Mg(\mu_0 - \Delta\mu s^*)$ is the braking torque necessary to stay at the maximum in the μ-slip curve. If $s(0) > s^*$ and the braking torque $M_B > M_B^* - \Delta\mu MgR[s(0) - s^*]$ we have $s(0) - A/B > 0$ and during the time interval Δt the slip will increase with $[s(0) - A/B]\exp(B\Delta t)$. Because $B\Delta t \sim 1/v_c$, the maximum slip will increase exponentially (until the wheel blocks, corresponding to $s = 1$)

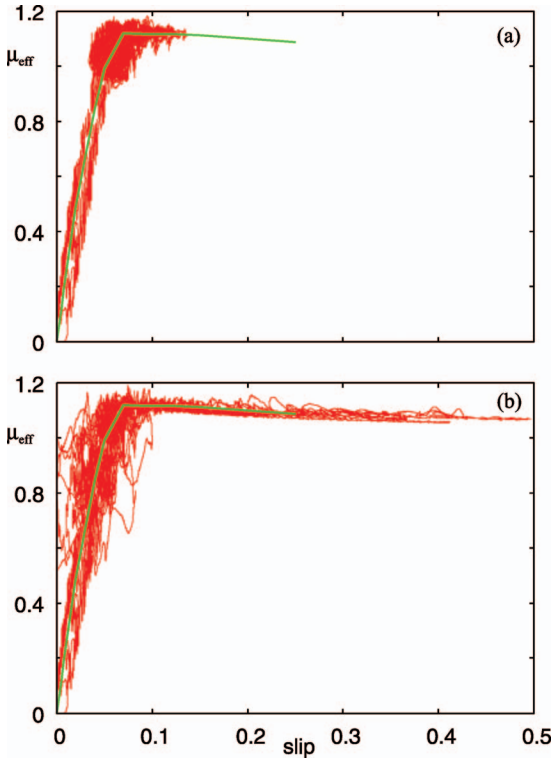

FIG. 38 — μ-*Slip curves for ABS braking using algorithms* ***a*** *(top) and* ***b*** *(bottom). The green curve is the steady-state* μ*-slip curve for car velocity* $\upsilon_c = 27$ *m/s, whereas the red curve shows the instantaneous effective friction coefficient.*

with the inverse of the car velocity. This behavior (i.e., the increase in the slip with decreasing car velocity) can be seen in Fig. 36b and Fig. 37b.

In Fig. 38, we show the μ-slip curve during stationary slip (green curve) and the instantaneous effective friction coefficient $\mu_{\text{eff}}(t) = F_x(t)/F_{\text{N}}$ during braking (red curve).

The red and green curves in Fig. 39 show the car velocity using the ABS control algorithms **a** and **b**. The ABS control algorithm **a** is slightly more effective than algorithm **b**, but algorithm **a** assumes that s^* is known and remains constant during the braking event.

In the calculations above for ABS algorithm **a**, we used $s^* = 0.05$ that, in fact, is not the maximum of the μ -slip curve that is instead at $s^* = 0.07$ (see Fig. 35). However, remarkably, the braking distance using $s^* = 0.07$ in the present case is almost the same as for $s^* = 0.05$ (see Fig. 40). The reason is that with the relative large magnitude of the brake moment change $\Delta M = 200$ Nm and the relative low frequency of the brake moment changes (time interval $\tau = 0.03$ s), algorithm **a** is

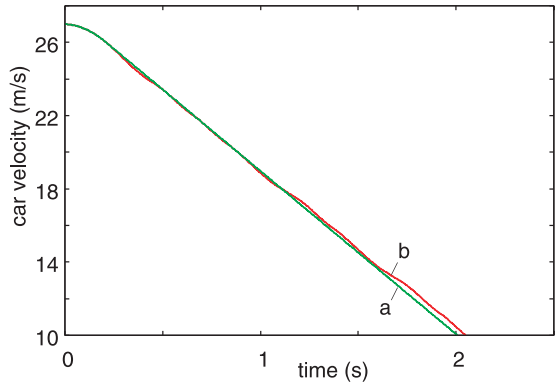

FIG. 39 — *Car velocity* v_c *as a function of time* t *during ABS braking using two algorithms* ***a*** *(with* $s^* = 0.05$*) and* ***b****. The procedures* ***a*** *and* ***b*** *result in nearly the same time,* $\approx$*2 s, for reducing the car velocity from 27 to 10 m/s. The effective friction* $\mu \approx 0.87$ *is smaller than the maximum kinetic friction (*$\approx$*1.1).*

not able to focus in on a narrow region of slip around s^*, but in each case fluctuates over a similar range of slip values as shown in Fig. 41. However, if we lower ΔM to 100 Nm and double the rate at which the brake moment is modified (so that $\tau = 0.015$ s), algorithm **a** results in a more narrow distribution of slip centered around s^*. This results in an increase in the braking distance for the case $s^* = 0.05$, whereas the braking distance for $s^* = 0.07$ is modified very little (see Fig. 42). In Fig. 43, we show the relation between the slip and the effective friction coefficient for the case where ΔM is 100 Nm and $\tau = 0.015$ s.

The ABS braking control algorithms used today usually assume that *only* the wheel rolling velocity $v_R(t)$ is known. Basically, whenever a wheel tends to lock up, which manifests itself in a large (negative) wheel angular acceleration, the

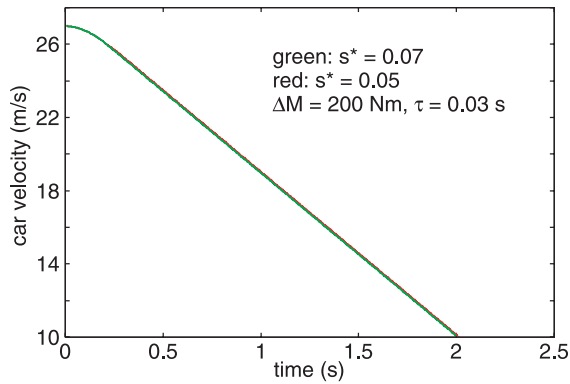

FIG. 40 — *Car velocity* v_c *as a function of time* t *during ABS braking using algorithm* ***a*** *with* $s^* = 0.05$ *and 0.07. Both cases result in nearly the same time for reducing the car velocity from 27 to 10 m/s. The effective friction* $\mu \approx 0.87$ *is smaller than the maximum kinetic friction (*$\approx$*1.1).*

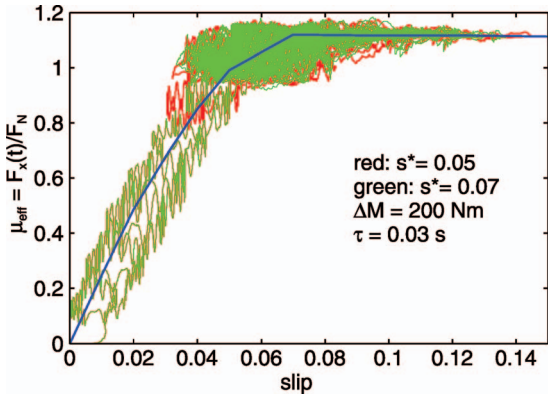

FIG. 41 — *Dynamical* μ*-slip curves for ABS braking using two different chosen* s**-slip values for control algorithm* ***a****. The blue curve is the steady-state* μ*-slip curve.*

braking torque is reduced. These ABS braking control algorithms (e.g., the Bosch algorithm) are rather complex and secret. The calculations presented above can be easily extended to such realistic ABS braking control algorithms and to more complex cases such as braking during load fluctuations (e.g., braking on uneven road surfaces) and switching between different road surfaces (by using different road surface power spectra during an ABS braking simulation).

Summary and Conclusions

Here, we have proposed a simple rubber friction law that can be used, e.g., in models of tire and vehicle dynamics. The friction law gives nearly the same result as the full rubber friction theory of Ref. [*6*], but it is much more

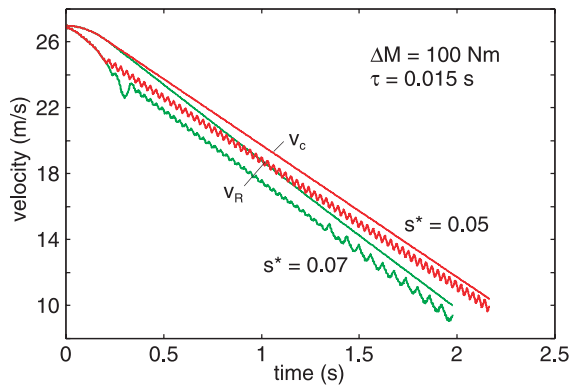

FIG. 42 — *Car velocity* v_c *and the rolling velocity* v_R *as a function of time* t *for ABS braking with two different chosen* s**-slip values using algorithm* ***a****.*

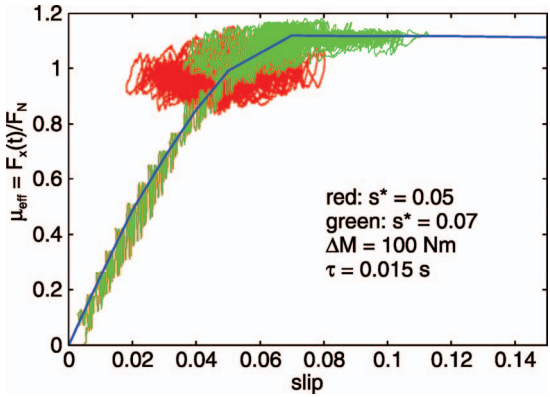

FIG. 43 — *Dynamical* μ*-slip curves for ABS braking using two different chosen* s**-slip values using algorithm* ***a****. The blue curve is the steady-state* μ*-slip curve.*

convenient to use in numerical studies of, e.g., tire dynamics, as the friction force can be calculated much faster.

We have presented a 2D tire model that combines the rubber friction law with a simple mass-spring description of the tire body. The tire model is very flexible and can be used to calculate accurate μ-slip (and the self-aligning torque) curves for braking and cornering or combined motion (e.g., braking during cornering). We have compared calculated results with experimental data from indoor tire dynamics measurements on sandpaper. Simulations of ABS braking were performed using two simple control algorithms.

Sandpaper is not an ideal substrate for comparisons to the tire model because of the relative sharp roughness, which results in much stronger wear than on asphalt or concrete road surfaces. In addition, the small roll-off wavelength, which was defined above, results in a rather different frictional behavior compared with asphalt or concrete road surfaces. Thus, in the future, it would be interesting to compare the tire model with outdoor measurements on real road surfaces, e.g. trailer tests.

References

[*1*] Persson, B. N. J., *Sliding Friction: Physical Principles and Applications*, 2nd ed, Springer, Heidelberg, Germany, 2000.

[*2*] Grosch, K. A., "The Relation between the Friction and Visco-Elastic Properties of Rubber," *Proceedings of the Royal Society of London Series A*, Vol. 274, 1963, pp. 21–39.

[*3*] Gent, A. N. and Walter, J. D., *The Pneumatic Tire*, U.S. Department of Transportation, Washington, D.C., 2006.

[*4*] Pacejka, H. B., *Tyre and Vehicle Dynamics*, 2nd ed, Elsevier, Amsterdam, The Netherlands, 2006.

[*5*] Persson, B. N. J., "Theory of Rubber Friction and Contact Mechanics," *Journal of Chemical Physics*, Vol. 115, 2001, pp. 3840–3861.

[6] Persson, B. N. J., "Rubber Friction: Role of the Flash Temperature," *Journal of Physics: Condensed Matter*, Vol. 18, 2006, pp. 7789–7823.

[7] Heinrich, G., Klüppel, M., and Vilgis, T. A., "Evaluation of Self-Affine Surfaces and their Implication for Frictional Dynamics as Illustrated with a Rouse Material," *Computational and Theoretical Polymer Science*, Vol. 10, 2000, pp. 53–61.

[8] Heinrich, G. and Klüppel, M., "Rubber Friction, Tread Deformation and Tire Traction," *Wear*, Vol. 265, 2008, pp. 1052–1060.

[9] Klüppel, M. and Heinrich, G., "Rubber Friction on Self-Affine Road Tracks," *Rubber Chemistry and Technology*, Vol. 73, 2000, pp. 578–606.

[10] Westermann, S., Petry, F., Boes, R., and Thielen, G., "Experimental Investigations Into the Predictive Capabilities of Current Physical Rubber Friction Theories," *Kautschuk, Gummi, Kunststoffe*, Vol. 57, 2004, pp. 645–650.

[11] Persson, B. N. J. and Volokitin, A. I., "Rubber Friction on Smooth Surfaces," *European Physical Journal*, Vol. E21, 2006, pp. 29–80.

[12] Carbone, G., Lorenz, B., Persson, B. N. J., and Wohlers, A., "Contact Mechanics and Rubber Friction for Randomly Rough Surfaces with Anisotropic Statistical Properties," *European Physical Journal*, Vol. E29, 2009, pp. 275–284.

[13] Persson, B. N. J., "On the Theory of Rubber Friction," *Surface Science*, Vol. 401, 1998, pp. 445–454.

[14] Le Gal, A. and Klüppel, M., "Evaluation of Sliding Friction and Contact Mechanics of Elastomers Based on Dynamic-Mechanical Analysis," *Journal of Chemical Physics*, Vol. 123, 2005, pp. 014704–014715.

[15] Persson, B. N. J., "Theory of Powdery Rubber Wear," *Journal of Physics: Condensed Matter*, Vol. 21, 2009, pp. 485001–485009.

[16] Mofidi, M., Prakash, B., Persson, B. N. J., and Albohr, O., "Rubber Friction on (Apparently) Smooth Lubricated Surfaces," *Journal of Physics: Condensed Matter*, Vol. 20, 2008, pp. 085223–085230.

[17] Persson, B. N. J., Albohr, O., Tartaglino, U., Volokitin, A. I., and Tosatti, E., "On the Nature of Surface Roughness with Application to Contact Mechanics, Sealing, Rubber Friction and Adhesion," *Journal of Physics: Condensed Matter*, Vol. 17, 2005, pp. R1–R62.

[18] Persson, B. N. J., Albohr, O., Creton, C., and Peveri, V., "Contact Area Between a Viscoelastic Solid and a Hard, Randomly Rough, Substrate," *Journal of Chemical Physics*, Vol. 120, 2004, pp. 8779–8794.

[19] Persson, B. N. J., "Rubber Friction and Tire Dynamics," *Journal of Physics: Condensed Matter*, Vol. 23, 2011, pp. 015003–015017.

[20] Persson, B. N. J., "Contact Mechanics for Randomly Rough Surfaces," *Surface Science Reports*, Vol. 61, 2006, pp. 201–230.

[21] Rodriguez, N. V., Masen, M. A., and Schipper, D.-J., "Tribologically Modified Surfaces on Elastomeric Materials," *Journal of Engineering Tribology*, Vol. 227, 2012, pp. 398–405.

[22] Kuhlmann, U. and Albohr, O., Pirelli Tire Company, personal communication.

[23] Lorenz, B., Persson, B. N. J., Fortunato, G., Giustiniano, M., and Baldoni, F., "Rubber Friction for Tire Tread Compound on Road Surfaces," *Journal of Physics: Condensed Matter*, Vol. 25, 2013, pp. 095007–095015.

[24] Press, W. H., Teukolsky, S. A., Vetterling, W. T., and Flannery, B. P., *Numerical Recipes*, 2nd ed., Cambridge University Press, 1992.